ACS Photonics

pubs.acs.org/journal/apchd5

Article

Unbiased Plasmonic-Assisted Integrated Graphene Photodetectors

Ioannis Vangelidis, Dimitris V. Bellas, Stephan Suckow, George Dabos, Sebastián Castilla, Frank H. L. Koppens, Andrea C. Ferrari, Nikos Pleros, and Elefterios Lidorikis*

Cite This: *ACS Photonics* 2022, 9, 1992−2007

Read Online

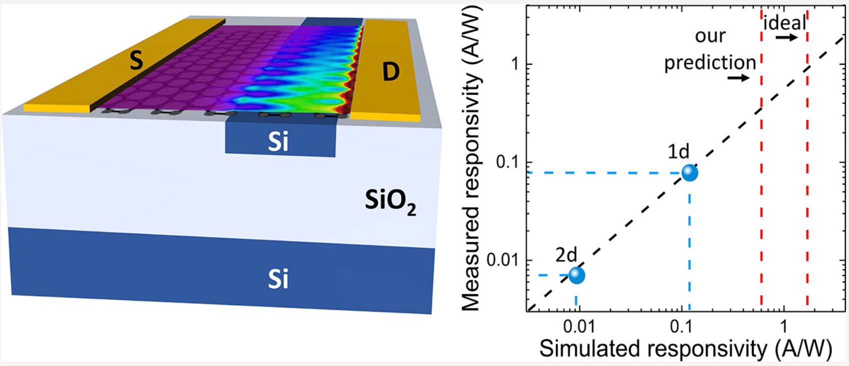

ABSTRACT: Photonic integrated circuits (PICs) for next-generation optical communication interconnects and all-optical signal processing require efficient (∼A/W) and fast (≥25 Gbs^{-1}) light detection at low (<pJbit^{-1}) power consumption, in devices compatible with Si processing, so that the monolithic integration of electro-optical materials and electronics can be achieved consistently at the wafer scale. Graphene-based photodetectors can meet these criteria, thanks to their broadband absorption, ultra-high mobility, ultra-fast electron interactions, and strong photothermoelectric effect. High responsivities (∼ 1 A/W), however, have only been demonstrated in biased configurations, which introduce dark current, noise, and power consumption, while unbiased schemes, with low noise and zero consumption, have remained in the ∼ 0.1 A/W regime. Here, we consider the unbiased asymmetric configuration and show that optimized plasmonic enhanced devices can reach for both transverse-electric and transverse-magnetic modes (at λ = 1550 nm), ∼A/W responsivity, and ∼ 100 GHz operation speed at zero power consumption. We validate the model and material parameters by simulating experimental devices and derive analytical expressions for the responsivity. Our comprehensive modeling paves the way for efficient, fast, and versatile optical detection in PICs with zero power consumption.

KEYWORDS: *graphene, photodetectors, integrated photonics, plasmonics, photothermoelectric effect*

INTRODUCTION

Photonic integrated circuits (PIC)[1] can be used for interconnects,[2,3] all-optical signal processing,[4,5] as well as for neuromorphic photonics,[6−8] whereby programmable (trainable) PICs become the photonic hardware counterpart for artificial neural network algorithms. There has been continuous progress in all key performance metrics,[9] including increased bandwidth (BW),[10] reduced footprint,[10] and reduced power consumption,[10] with current transceiver technologies already allowing for 400 Gb/s operation,[3] and moving towards 800 Gbs^{-1}[9] and 1.6 Tbs^{-1} interconnect applications.[2]

With receiver circuitry forming a critical element in the landscape of PICs, this performance race confronts the photodetector (PD) technology with a challenging functionality framework. PDs must constantly aim for smaller-size layouts with high optoelectronic BW (>100 GHz)[11] and improved efficiencies (∼ 1 A/W),[12,13] while expanding along a complementary metal-oxide-semiconductor (CMOS) process compatible framework.[14] At the same time, they are required to operate at a low energy envelope, with improved noise characteristics,[10] thus making a strong case for unbiased operational schemes which have zero power consumption, zero dark current, and low noise.[15] They also need to support dynamic tunability in both photoresponse and electrical resistance, when their employment in balanced-PD schemes is targeted, i.e. paired PDs of equal response with their signal subtracted to reduce the light source noise,[16−18] or subtraction of mixed signals in coherent detection schemes.[19] Currently used bulk semiconductor technologies such as Ge[20,21] and

Received: January 17, 2022
Published: June 2, 2022

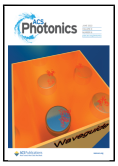

https://doi.org/10.1021/acsphotonics.2c00100

InP[22,23]-based PDs cannot meet all these criteria simultaneously. Besides spectral limitations associated with the semiconductor band gap,[24] they often enforce process changes[20,21,24,25] or experience speed limitations due to the material intrinsic mobility and increased thickness of the photoactive layer.[26] These factors led to PD devices with increased complexity,[26] and a trade-off between operation speed and responsivity.[27]

Single-layer graphene (SLG) is ideally suited to meet the abovementioned requirements,[10,15,28−30] and a variety of integrated graphene PD (GPDs) prototypes have been demonstrated.[31−45] SLG exhibits ultrafast electron interactions (<50 fs),[46] extremely high room temperature (RT) carrier mobilities (>10,000 cm^2/Vs),[47−51] CMOS compatibility,[15,52,53] field-effect gate tunability,[54−57] and broadband optical response.[28,29,58,59] On-Chip GPDs have been reported in both biased[31,34,36,40−42,45] and unbiased[34−40,44] schemes, demonstrating external responsivity (i.e. ratio of photocurrent I_{ph} to incoming power P_{in}) up to $R_{\mathrm{I,ext}} \sim 0.7$ A/W[42] and ~ 0.11 A/W,[44] respectively, at $\sim$ 100 Gb^{-1}.[31,41,45] In a biased scheme, a source−drain voltage is applied to SLG and the photocurrent is measured as the difference between bright (under illumination) and dark currents,[31] where the bright current is modulated as a result of photoconductive[36,60] and photobolometric[31,60] effects. Under bias, however, the SLG gapless nature[61] leads to a sizable dark current and increased noise,[15] resulting in a non-negligible power budget for PD operation ($\sim$ 1 mW)[31] and for the overall power requirements.[15] Lower power metrics, on the other hand, can be accomplished when PDs operate without bias[15,28] exploiting the photothermoelectric (PTE) effect,[28,30] whereby an electronic temperature, T_{e}, gradient gives rise to a photovoltage due to the Seebeck effect.[62] To get a net photoresponse from the device, the symmetry between source and drain contacts must be broken. This can be achieved by either an architecture supporting asymmetric light absorption,[33−35] or by an asymmetric gate creating a lateral pn-junction configuration.[36−40,44]

Unbiased GPDs reported so far have been typically augmented with absorption enhancement mechanisms to increase the SLG absorption above the 2.3%[58] it has when suspended and even lower on a substrate,[63] exploiting either photonic crystals[40] or plasmonics.[32,37,41] However, thus far, $R_{\mathrm{I,ext}} \lesssim 0.11$ A/W for unbiased devices,[34,36,40,44] significantly lower than the $\sim$ 0.7 A/W reported for biased GPDs.[42] Given the preference for zero dark current, low noise, and low power consumption in PIC PDs, the critical question, then, is whether $R_{\mathrm{I,ext}} \sim 1$ A/W or above can be obtained in unbiased GPDs.

Here, we show that this is possible, by analyzing the performance of a device architecture consisting of unbiased source−drain contacts asymmetrically placed with respect to a Si waveguide (WG).[33−35] We employ coupled optical, thermal, and electrical simulations, and show that the simplest design enables strong (i.e., $R_{\mathrm{I,ext}} \sim 1$ A/W) performance even at zero bias. We provide realistic full device model and material parameters, validated by comparison to experimental results. This allows us to understand the photoresponse mechanisms, the reasons why prior art reached different results and smaller performance, and how to optimize device concepts and designs (i.e., plasmonic effects at the contact edge, WG and contact configurations, and gating profile). An analytical expression derived for the ideal PTE performance (where absorption occurs only in SLG within a delta distribution at the contact edge without metal losses) defines an ideal internal responsivity (i.e., the ratio of photocurrent I_{ph} to absorbed power P_{abs}) limit up to few A/W for asymmetric-contact unbiased GPDs. We consider both transverse electric (TE) and transverse magnetic (TM) guided modes. A scan of different gating combinations shows that independent dynamic control of resistance and $R_{\mathrm{I,ext}}$ can be achieved, paving the way to balanced photodetection schemes.[16−18] Noise, sensitivity, and operation speed metrics are also calculated.

Our comprehensive theoretical framework provides the understanding and guidelines needed to have tunable integrated GPDs with zero-consumption, low-noise, high-sensitivity, and high-speed operation.

■ RESULTS AND DISCUSSION

We consider an integrated GPD comprising a Si WG (220 nm thick) on a silicon-on-insulator substrate, as shown in Figure 1.

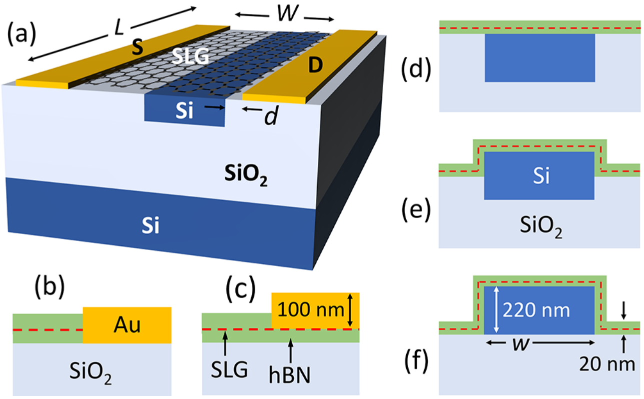

Figure 1. (a) Schematic device configuration with Si WG (220 nm thick) fully embedded in the SiO$_2$ substrate (the encapsulating hBN layers are not shown for clarity). (b,c) Schematic 1d (edge) and 2d (top) contacts, respectively. (d−f) Schematics of 3 WG configurations: fully embedded in SiO$_2$, half embedded, and fully exposed, respectively.

hBN encapsulation ensures high-mobility SLG at RT.[64] Two Au electrodes (100 nm thick) are located asymmetrically on opposite sides of the Si WG to collect the photocurrent assuming unbiased operation: one of them 700 nm off the WG edge, and the other at a distance d, varied between 300 and −100 nm. Two contact formats are explored: 1d edge contact[65,66] (Figure 1b) and 2d top contact[66,67] (Figure 1c). Three Si WG configurations are also explored: fully embedded[34] (Figure 1d), half-embedded[35] (Figure 1e), and exposed (Figure 1f). The WG width, w, and device length, L, are varied, while all other parameters in Figure 1 remain fixed.

In unbiased metal/GPD devices, both PTE[34,68,69] and photovoltaic[68−71] mechanisms contribute to the photoresponse, depending on contact metals[72,73] and light polarization.[69,72] In an asymmetric device configuration, like that studied here, photocurrent measurements as a function of top-gate and source−drain voltages indicated PTE as the dominant effect.[34] Thus, we also assume it to be the dominant mechanism here. Its traits include ultrafast detection[36,39] and zero-bias operation,[15,28,74,75] the latter providing for low noise[10,15] and low power consumption.[10,15] The PTE effect generates a voltage drop (thus an internal field) $V_{\mathrm{PTE}} \propto s\nabla T_{\mathrm{e}}$,[72,74] where the Seebeck coefficient, s, depends on T_{e} and Fermi level, E_{F}, across the SLG channel, with no requirement of a source−drain bias to observe an ultrafast re-

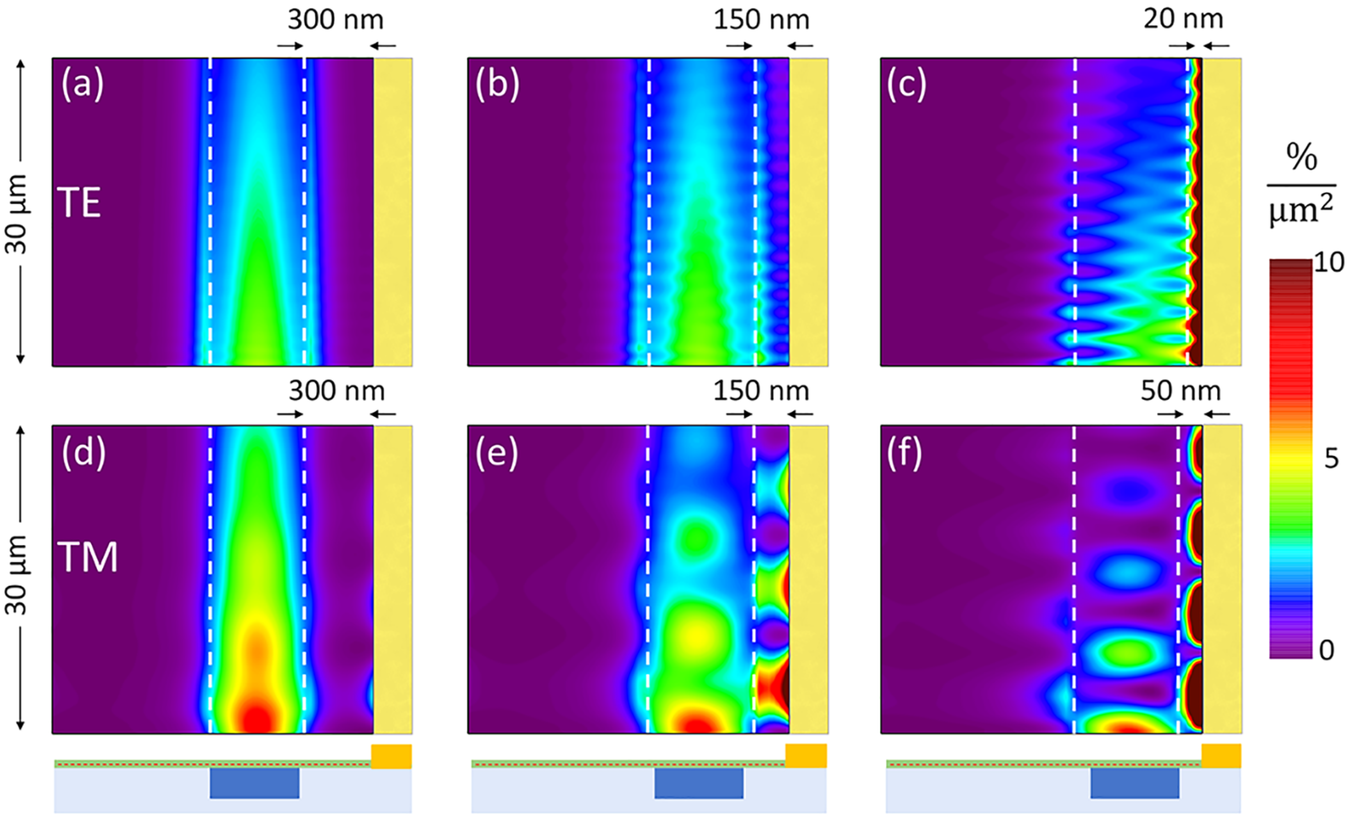

Figure 2. Absorption density α_{den} (%/μm^2) in SLG channel for (a−c) TE and (d−f) TM mode at λ = 1550 nm, at different d. The other contact is 700 nm to the left of the figures (not shown). The device configuration is 1d contact, w = 450 nm, L = 30 μm, and fully embedded Si WG. The white dashed lines indicate the Si WG position and the yellow bar the Au contact.

sponse.[34,35,37,39] For obtaining a net nonzero V_{PTE} without bias, an asymmetry must be present in $s(x)$ or in $\nabla T_e(x)$, where x runs from source to drain. The former can be achieved by a split-gate to create an in-plane pn-junction.[36−40,44] The latter, simpler and employed here, is achieved by asymmetrically positioning the contacts with respect to the Si WG.[33−35]

Full-wave simulations, for both the fundamental TE and TM modes at λ = 1550 nm, incident from the Si WG into the PD, in Figure 2, show the emerging optical effects as one of the contacts is brought closer to the WG. The optical mode excites and hybridizes with surface plasmon polaritons (SPP) on the Au contact edge,[33] increasing the local SLG absorption. The hybridization is seen by the beating pattern of the absorption along the WG, becoming more pronounced as d decreases, and creating a strong asymmetry in the SLG absorption profile. This increases T_e locally, while close to the other contact SLG remains cold. Note, however, that roughness on the metal contact will add to scattering and propagation losses on the plasmon mode, reducing SLG absorption, thus limiting the benefits coming from the SPPs.

The SLG electron (e) heating and cooling dynamics can be understood as follows: light absorption creates hot non-equilibrium carriers which undergo carrier multiplication by electron−electron (e−e) scattering ($\tau_{\mathrm{e-e}}$ < 50 fs),[46,76,77] i.e., by impact ionization (interband scattering creating new e-h pairs[78,79]) and impact excitation (intraband scattering distributing the excess energy within the band[80]) and relax into a hot equilibrium Fermi−Dirac carrier distribution at an elevated temperature T_e.[46,76,77,81,82] This hot thermalized carrier distribution is established locally with one temperature (T_e) and chemical potential (μ).[46,77] Local cooling of the e gas then follows, by electronic heat diffusion and electron−phonon (e−ph) scattering ($\tau_C \sim$ 2−4 ps).[46,82−89] Due to the much smaller SLG electronic heat capacity compared to the ones of SLG lattice, hBN, and metal contacts,[90] the latter are assumed to remain at RT. Also, plasmonic hot carrier (HC) effects[91,92] in the Au contacts have a small effect on the PTE response (see Methods). Considering all this, heat diffusion simulations (see Methods) show that the absorption spatial asymmetry results in a T_e asymmetric profile, which, in turn, gives rise to a thermoelectric voltage[74] $V_{\mathrm{PTE}} = L^{-1}\int_0^L \int_0^W s\nabla T_e \, dx \, dy$, where the integration is over the entire SLG area (length L and width W). V_{PTE} is the device's open-circuit voltage. The performance metric is the voltage external responsivity $R_{\mathrm{V,ext}} = V_{\mathrm{PTE}}/P_{\mathrm{in}}$, where P_{in} is the incoming optical power. If the device internal resistance is R_D, then the external sort-circuit current responsivity is $R_{\mathrm{I,ext}} = R_{\mathrm{V,ext}}/R_D$. We note that in either open-circuit or sort-circuit conditions, the output power efficiency of the device is zero. We now consider the effects of WG, contacts, device geometries, and SLG doping to reach a generalized understanding of the PTE effects in integrated GPDs and, by that, an optimization framework.

We first examine the SLG E_F effect. We assume it pinned at −0.15 eV at/under the contacts (because of charge flow between SLG and metal reaching an equilibration depending on the metal work function),[93] while it can vary across the channel (source-to-drain). Typically, SLG is found to be p-doped.[94] We consider 3 indicative E_F = −0.02, −0.10, −0.18 eV, corresponding to extremely low, low, and average doping for hBN encapsulated SLG, respectively.[95,96] Figure 3a plots the distribution of T_e increase within the SLG channel for a d =

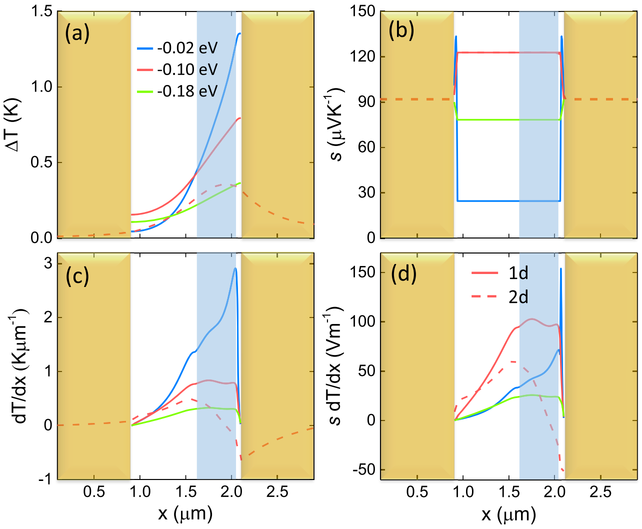

Figure 3. Spatial distribution of thermal quantities across SLG channel at the front (entrance) of the device for 1 μW incoming power with d = 50 nm, L = 30 μm, TE polarization, and fully embedded Si WG configuration. Solid lines correspond to various SLG E_F for a 1d contact, while the dashed line corresponds to E_F = −0.1 eV for a 2d contact. E_F is assumed fixed at −0.15 eV under the contacts. (a) T_e increase, (b) s, (c) T_e gradient, and (d) local thermoelectric voltage $s\nabla T_e$ projected along the x (source−drain) direction. In all panels, the yellow bars indicate the Au contacts, and shaded light blue the Si WG.

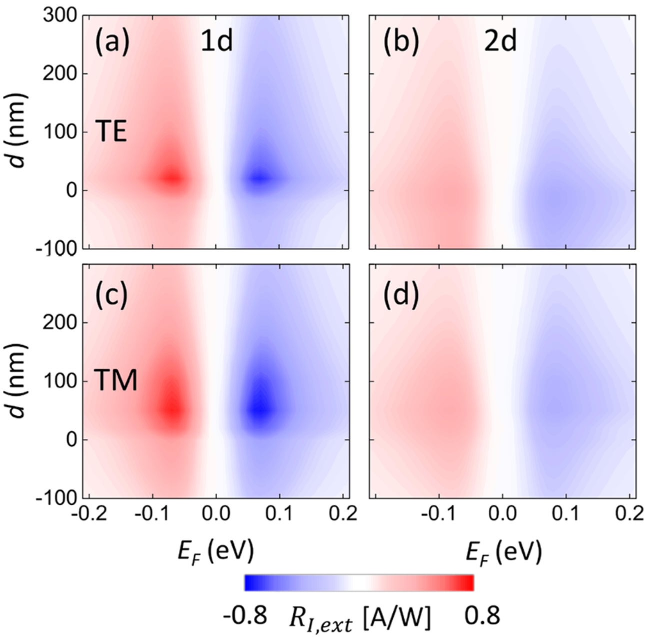

Figure 4. $R_{\mathrm{I,ext}}$ [A/W] as a function of SLG E_F and d for (a,b) TE and (c,d) TM modes. (a,c) 1d and (b,d) 2d contacts. Calculations are for fully embedded Si WG, with w = 450 nm and L = 30 μm.

50 nm and L = 30 μm device illuminated with TE polarization at 1 μW. The absorption profile is practically the same for any E_F in the range −0.21 to 0.21 eV, but differences in heat capacity and thermal conductivity (see Methods) result in different T_e profiles. In addition, the different E_F gives different s (see Methods). As shown in Figure 3c,d, the profile and peak position of the thermoelectric voltage are determined by the T_e gradient, while s determines the magnitude. Thus, while E_F = −0.10 eV does not produce the largest T_e gradient (see Figure 3c), it does yield the largest thermoelectric voltage due to the larger s, as for Figure 3b.

The main difference between 1d and 2d contacts is that in the latter SLG extends under them,[66] providing extra space for cooling through electronic heat diffusion and e−ph scattering. In the 1d case, in contrast, the electronic heat diffusion process is terminated at the contact edge, which results in a larger T_e gradient, thus higher $R_{\mathrm{I,ext}}$. Cooling can be faster (i.e., smaller τ_C) locally where SLG is directly contacted by Au[97,98] (due to interactions with Au's e and ph or due to resonant dissipation from atomic defects along the SLG edges[99]). This affects the performance of both 1d and 2d contacts. We will start by assuming τ_C to be everywhere the same, so to derive an upper limit for the performance, then consider the effects of faster cooling at the contacts.

To systematically optimize d and E_F, we continuously vary them within the range −100 nm < d < 300 nm and −0.21 eV < E_F < 0.21 eV. The unbiased $R_{\mathrm{I,ext}}$ is plotted in Figure 4 for both polarizations (TE and TM) and both contact geometries (1d and 2d) for the fully embedded Si WG configuration. 1d is better than 2d in all the parameter space. $R_{\mathrm{I,ext}}$ increases as d is reduced, reaching an optimum at d = 20 nm and d = 50 nm for TE and TM polarizations, respectively (see Figure 2c,f), where the best compromise between plasmonic field confinement and losses is achieved (see Figure 4 and Methods). If the contact gets closer than this optimal d or overlaps with the WG (i.e., d < 0), $R_{\mathrm{I,ext}}$ drops sharply due to increased metal absorption and scattering of the mode on the Au contact edge (see Methods). We note that ref 100 presented the case of complete overlap between contact and underlying WG (i.e., d < −450 nm), reporting $R_{\mathrm{I,ext}}$ ∼ A/W as a result of optimistic SLG property values (i.e., heat capacity c_e ∼150 J m^{-3} K^{-1} and cooling time τ_C ∼ 10 ps; thus interfacial heat conductance $\Gamma_{\mathrm{cool}} = c_e/\tau_C \sim 5 \times 10^3$ W m^{-2} K^{-1} ∼ 10 times smaller than our ∼5×10^4 W m^{-2} K^{-1}, and also zero contact resistance). Indeed, simulating the ref 100 structure using their parameters we reproduce their findings, but with our SLG property assumptions, we obtain $R_{\mathrm{I,ext}}$ < 0.1 A/W, which is in line with Figure 4. We stress that the use of improper SLG parameters can lead to erroneously inflated responsivities, e.g, ∼ 1000 A/W in ref 101 (here τ_C ∼ 5 ns was used, instead of the experimentally measured τ_C ∼ 3 ps,[46,82−89] and zero contact resistance). For TM, the response is less sensitive to d, due to the more extended fields and stronger coupling with the Au SPPs, as evident in Figure 2. For both cases, the optimal E_F = ±0.07 eV. This is the optimal point of two counter-acting trends: at smaller E_F, s drops sharply. At larger E_F, thermal conductivity and thermal capacity increase (see Methods) resulting in reduced T_e gradients.

We now consider the 1d contacts, E_F = −0.07 eV, and perform optimization simulation runs, shown in Figure 5 for both TE and TM polarizations. The effect of Si WG position with respect to the top oxide surface is shown in Figure 5a,b for two d. The fully embedded configuration is the optimal one for both polarizations. This is also easier to fabricate because the device is on a flat substrate. In Figure 5c,d, the effect of w is studied, assuming the fully embedded configuration. Different trends are observed between the two polarizations. For the optimal d = 20 and 50 nm for TE and TM, the peak $R_{\mathrm{I,ext}}$ is observed at w = 350 and 450 nm, respectively. Narrowing the WG width results in vanishing $R_{\mathrm{I,ext}}$ for TM, but not for TE. In both cases, detuning from the optimal w degrades $R_{\mathrm{I,ext}}$. A

https://doi.org/10.1021/acsphotonics.2c00100
ACS Photonics 2022, 9, 1992−2007

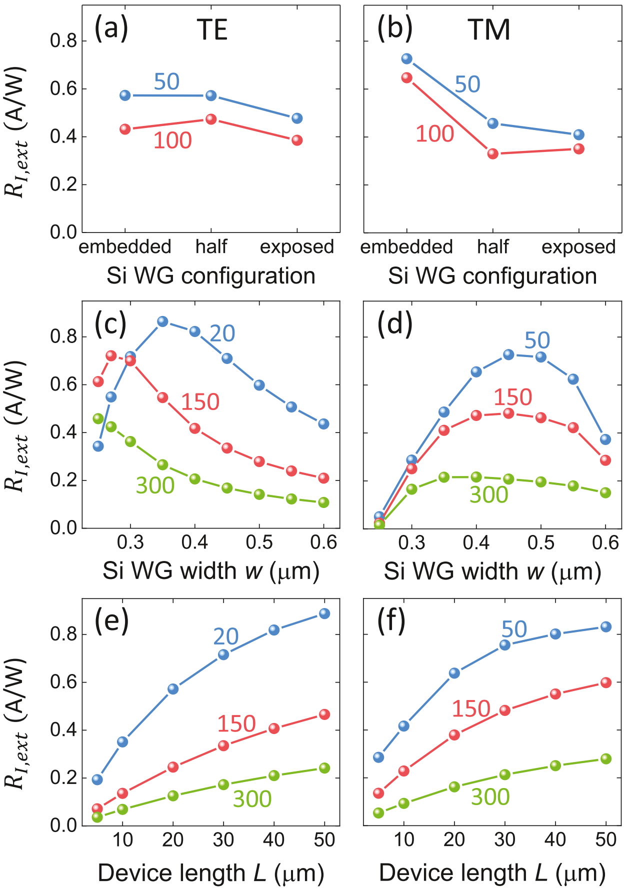

Figure 5. $R_{\mathrm{I,ext}}$ (A/W) for SLG E_{F} = −0.07 eV at 1d contact configuration, as a function of (a,b) WG embedding (at L = 30 μm and w = 450 nm), (c,d) w (fully embedded Si WG and L = 30 μm), (e,f) L (fully embedded Si WG and w = 450 nm). The numbers on the curves indicate different d. Panels (a,c,e) are for TE and (b,d,f) for TM mode.

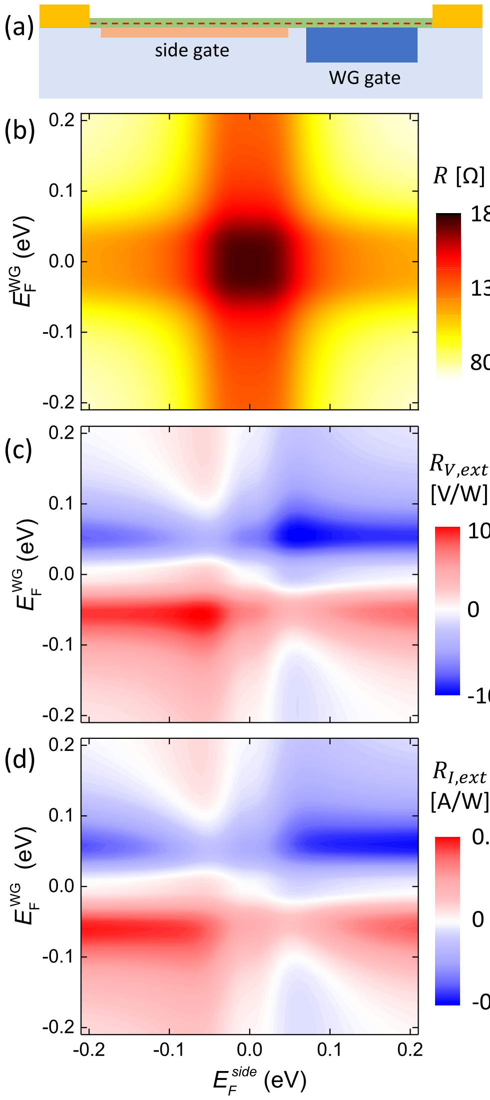

Figure 6. (a) Schematic double-gating architecture, employing a WG gate and a side gate. (b) Resistance, (c) $R_{\mathrm{V,ext}}$ [V/W], and (d) $R_{\mathrm{I,ext}}$ [A/W] as a function of SLG "WG" and "side" E_{F}, for the TE mode, d = 20 nm, L = 30 μm, w = 450 nm, 1d contact and fully embedded Si WG.

wider WG spreads out the mode, and a narrower WG reduces mode confinement, both cases resulting in smaller T_{e} gradients.

Figure 5e,f shows the effect of device length. The trends in TE and TM polarizations are very similar, with a monotonic $R_{\mathrm{I,ext}}$ increase for longer devices. This is due to larger overall absorption and smaller SLG channel resistance. An opposite trend is observed for the external voltage responsivity $R_{\mathrm{V,ext}}$ (i.e., photovoltage V_{ph} to incoming power P_{in}[30]), where the higher absorption density in the device entrance promotes a larger $R_{\mathrm{V,ext}}$ for shorter devices (see Methods).

The dependence of PTE response on SLG E_{F} opens a new avenue for dynamic control of both resistance and responsivity, towards a balanced photodetection scheme.[16−19] This is an established method to reduce the effect of intrinsic light-source noise.[16] A simple embodiment is realized by two PDs of equal $R_{\mathrm{I,ext}}$, whereby subtraction of their photocurrents removes the excess noise.[16] The balanced PD pair output remains zero until a signal difference causes an "unbalance", thus a net output.[16] Balanced PDs are also essential in coherent detection schemes,[19] which can significantly increase the transmission capacity by using the phase, amplitude, and polarization of the optical signal to carry information.

Figure 6a shows a schematic concept in which the Si WG is used as a gate, and a secondary gate is inserted on the side (we assume it does not affect the optical mode or the SLG absorption profile). The device has L = 30 μm, 1d contact layout, fully embedded WG, w = 450 nm, and d = 20 nm, at TE polarization. The device resistance R_{D} as a function of WG and side SLG E_{F} is in Figure 6b, while the corresponding $R_{\mathrm{V,ext}}$ and $R_{\mathrm{I,ext}}$ are in Figure 6c,d, respectively. Under these assumptions (see Methods), R_{D} = 130 ± 50 Ω (∼ ± 40% change) as V_{G} varies. A sixfold pattern emerges, typical of PTE,[62] with values ranging between 0 and ∼100 V/W or 0 and ∼0.9 A/W for $R_{\mathrm{V,ext}}$ and $R_{\mathrm{I,ext}}$, respectively. $R_{\mathrm{V,ext}}$ increases further for shorter L, as shown in Methods, where it can exceed 200 V/W.

The operational optimal is at $E_{\mathrm{F}}^{\mathrm{WG}} = E_{\mathrm{F}}^{\mathrm{side}} = \pm 0.06$ eV for $R_{\mathrm{V,ext}}$, reaching up to 102 V/W, but at $E_{\mathrm{F}}^{\mathrm{WG}} = \pm 0.06$ eV, $E_{\mathrm{F}}^{\mathrm{side}} = \pm 0.2$ eV for $R_{\mathrm{I,ext}}$, reaching up to 0.88 A/W. The reason is as follows: the SLG E_{F} above the WG (where the highest T_{e} gradients are found) needs to be $E_{\mathrm{F}}^{\mathrm{WG}} = \pm 0.06$ eV. Increasing the side $|E_{\mathrm{F}}| > 0.06$ eV results in s reduction, as well as electrical resistance reduction (see Methods). This translates into a reduced (because of s) thermoelectric voltage ($R_{\mathrm{V,ext}}$ reduction), but with a marginally increased (because of resistance) thermoelectric current ($R_{\mathrm{I,ext}}$ increase). In either case, the independent variation of $E_{\mathrm{F}}^{\mathrm{WG}}$ and $E_{\mathrm{F}}^{\mathrm{side}}$ can enable independent dynamic control of R_{D}, and $R_{\mathrm{V,ext}}$, towards balanced photodetection.

$R_{\mathrm{V,ext}}$ and $R_{\mathrm{I,ext}}$ assume open-circuit and short-circuit conditions, respectively,i.e., no power is transferred out of the system. It is instructive to extrapolate to the case of an external load R_{L} closing the circuit with $R_{\mathrm{L}} = R_{\mathrm{D}}$, the condition for maximum power transfer efficiency, whose ideal value is $\eta_{\max} = V_{\mathrm{PTE}}{}^2/4R_{\mathrm{D}}P_{\mathrm{in}}$.[102] For $P_{\mathrm{in}} = 1\ \mu$W, we find $\eta_{\max} \sim 0.002\%$ at $R_{\mathrm{V,ext}} = 100$ V/W and $R_{\mathrm{D}} = 120\ \Omega$. Within the linear regime, $\eta_{\max}$ increases with increasing P_{in}. In ref 44, the linear regime extended up to $P_{\mathrm{in}} = 0.1$ mW, beyond which the responsivity dropped as $P_{\mathrm{in}}{}^{-1/3}$ due to SLG's nonlinear response to temperature.[76,86,103] Scaling our findings to the ref 44 trends, we get $\eta_{\max} \sim 4\%$ at $P_{\mathrm{in}} = 1$ W. These are upper limits. Full device circuit modeling is needed for accurate evaluations.[104]

Until now, we made the simplifying assumption that Au contacts do not affect the e local cooling rate in SLG at (or under) the contacts, and assumed a fixed $\tau_{\mathrm{C}} \sim 3$ ps[34,75] everywhere. However, it is expected that Au ph and e may increase locally the SLG e cooling rate.[97,98] The Au e−e and e−ph thermalization times were estimated in the 1−3 ps regime by theoretical[105,106] and experimental[107−111] works, with the smallest reported value ∼ 0.25 ps.[110] Another source of increased cooling could be related to roughness in the metal contact. For the 1d case, on the other hand, increased cooling near the contact could originate by resonant dissipation from atomic defects along the SLG edge.[99] To evaluate the effect of increased scattering, we assume a locally reduced cooling time $\tau_{\mathrm{C}}^{\mathrm{red}}$ in SLG under the contact and up to a distance δ away from it (for the 1d contact $\tau_{\mathrm{C}}^{\mathrm{red}}$ involves only this δ). In the absence of experimental δ values, we assume, for simplicity and without loss of generality, $\delta = 25$ nm as used in ref 98. $\tau_{\mathrm{C}}^{\mathrm{red}}$ also lacks an experimental value, so it is used here as a free parameter. Simulations with $\tau_{\mathrm{C}}^{\mathrm{red}}$ reduced to 0.1 ps are shown in Figure 7 for the fully embedded TE mode case, with SLG $E_{\mathrm{F}} = -0.07$ eV, $d = 20$ nm, $L = 30\ \mu$m, and $w = 450$ nm. $R_{\mathrm{I,ext}}$ drops for smaller $\tau_{\mathrm{C}}^{\mathrm{red}}$, but at a faster rate for 2d compared to 1d contacts.

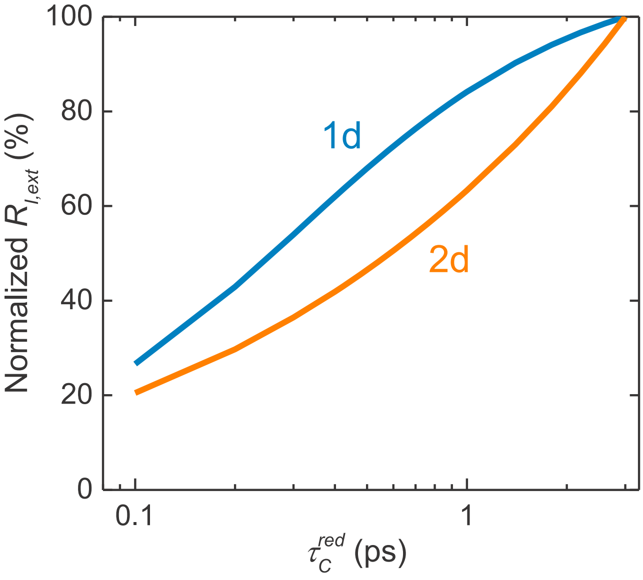

Figure 7. $R_{\mathrm{I,ext}}$ as a function of $\tau_{\mathrm{C}}^{\mathrm{red}}$ in SLG at/under the metal contact, normalized to $R_{\mathrm{I,ext}}$ when $\tau_{\mathrm{C}}^{\mathrm{red}} = 3$ ps.

This trend is reversed when $\tau_{\mathrm{C}}^{\mathrm{red}}$ approaches 0.1 ps. $R_{\mathrm{I,ext}}$ reduces by 32% and 54% at $\tau_{\mathrm{C}}^{\mathrm{red}} = 0.5$ ps for the 1d and 2d cases, respectively. Thus, an increased e cooling rate at the contacts will impose a significant $R_{\mathrm{I,ext}}$ reduction, more strongly for the 2d case, without however altering the main predictions of our work (see Methods).

We next validate our results by comparing our model findings with the measurements of two similar devices, ref 35, where 2d contacts were used, and ref 34, where 1d ones were used (both in TE polarization). Simulations are done using the experimental device geometries of refs 34 and 35 detailed in Table 1. In the 2d case[35] some missing information is assumed: in the experiment, there was no gate on SLG, so we assume p-doping $E_{\mathrm{F}} = -0.14$ eV.[94,112] We assume $\mu_{\mathrm{q}} = 2000$ cm^2/Vs as for ref 45, and a unit length contact resistance $\rho_{\mathrm{C}} = 1.2$ kΩ μm.[67] For the 1d case,[34] we assume $\mu_{\mathrm{q}} = 7000$ cm^2/Vs and $\rho_{\mathrm{C}} = 0.5$ k $\Omega\mu$m[65] (in ref 34 $\mu_{\mathrm{q}} = 1000$ cm^2/Vs was estimated, but with the effect of contact resistance integrated into the mobility), which, at the optimum $|E_{\mathrm{F}}| \sim 0.1$ eV, yield $R_{\mathrm{D}} \sim 93$ Ω, very close to the experimental value. For both contacts, we assume the same $\tau_{\mathrm{C}} = 3$ ps and $\tau_{\mathrm{C}}^{\mathrm{red}} = 0.5$ ps. Using the assumptions of Table 1, we reproduce the experimental resistance and $R_{\mathrm{I,ext}}$ of refs 34 and 35. The final agreement between simulated and measured results confirms the validity of our model. A common $\tau_{\mathrm{C}}^{\mathrm{red}} = 0.5$ ps assumption is adequate for both contact designs, confirming that there is faster cooling of SLG e at the metal contact. Small discrepancies between experiments and models can be due to a variety of reasons. Thus, rather than fitting $\tau_{\mathrm{C}}^{\mathrm{red}}$ to coerce an exact agreement, we adopt $\tau_{\mathrm{C}}^{\mathrm{red}} = 0.5$ ps as a reasonable assumption.

This confirms that $R_{\mathrm{I,ext}} \sim 0.6$ A/W is possible, for $L = 30$ μm with the faster $\tau_{\mathrm{C}}^{\mathrm{red}} = 0.5$ ps at the contacts. In terms of external quantum efficiency (collected e−h pairs to incoming photons ratio[30]): EQE = $R_{\mathrm{I,ext}}hc/e\lambda \sim 48\%$. By considering the simulated SLG absorption $\alpha_{\mathrm{SLG}} \sim 50\%$ (∼ 30% transmission and ∼ 20% scattering and parasitic contact absorption losses) in our best design, we get an internal quantum efficiency (collected e−h pairs to absorbed photons ratio[30]) IQE ∼ 100%. We note that high IQE (even >100%) are a result of carrier multiplication, i.e., the creation of multiple HCs per absorbed photon.[46,76,77,81,82] HC multiplication and carrier heating is very efficient in SLG,[77] and can be exploited for various applications.[77]

To put these numbers in perspective, we derive the ideal internal PTE performance (responsivity and quantum efficiency) to set a theoretical upper limit of an asymmetric contact architecture. We make two assumptions: (a) absorption occurs only in SLG (no scattering or metal absorption) and (b) absorption occurs in a δ-distribution width at the contact edge (maximized field confinement). Assuming that ΔT_{e} exponentially decays in both x (along the source−drain) and y (along the WG) directions, its profile is given by:

$$\Delta T_{\mathrm{e}} = \Delta T_{\mathrm{e}}^{0} \mathrm{e}^{-y/\psi} \mathrm{e}^{-x/\xi} \tag{1}$$

where $\Delta T_{\mathrm{e}}^{0}$ is the peak T_{e} rise, $\xi = \sqrt{\kappa\tau_{\mathrm{C}}/c_{\mathrm{e}}}$ [m] is the cooling length across the SLG channel, and ψ is the decay length due to SLG absorption along the WG length (used as a free parameter). κ and c_{e} are the SLG heat conduction and capacity, respectively. For a long device ($L \gg \psi$), all light is absorbed, and we get the ideal internal current responsivity (see Methods):

Table 1. Setup of Selected Experimental Devices (TE Polarization)[34,35] and Comparison between Measurements and Simulations

	contact type	1d[34]	2d[35]	
device setup	device length L	40	30	μm
	S−D distance W	3	1.4	μm
	contact distance d	0.2	0.3	μm
	WG width w	0.52	0.4	μm
	SLG-Si spacer thickness	35	25	nm
	electron cooling time τ_C	3	3	ps
	carrier mobility μ_q	7000[a]	2000[a]	cm^2/Vs
	residual local charge n_0*	3[b]	7[b]	$(\times 10^{11})$ cm^{-2}
	graphene Fermi level E_F	−0.11	−0.14[a]	eV
	contact resistance ρ_C	0.5[a]	1.2[a]	kΩ μm
measurements[34,35]	graphene absorption α_{SLG}	40	35	%
	device resistance R_D	96	187	Ω
	current responsivity $\boldsymbol{R}_{I,ext}$	0.078	0.007	A/W
simulations	graphene absorption a_{SLG}	40	37	%
	device resistance R_D	93	187	Ω
	current responsivity $\boldsymbol{R}_{I,ext}$	0.12	0.0094	A/W

[a]Assumed based on reported SLG quality and device resistance. [b]Estimated by the linear relation between $1/n_0^*$ and μ_q according to ref 113 (see Methods).

$$R_{I,int}^{\infty} = gs/\beta \tag{2}$$

while for the smallest length ($L \to 0$) we get the ideal voltage responsivity:

$$R_{V,int}^{0} = s/\beta\psi \tag{3}$$

where g [Ω^{-1} m^{-1}] is the device electrical conductance per unit length, and $\beta = \sqrt{c_e\kappa/\tau_C}$ [W/mK] is a generalized heat exchange coefficient. For our SLG parameters (E_F = −0.07 eV, τ_C = 3 ps, and μ_q = 10,000 cm^2/Vs) for ideal (nonabsorbing) 1d contacts we find $R_{I,int}^{\infty} \sim 2.5$ A/W (∼ 1.7 A/W if we include the 32% reduction at $\tau_C^{red} = 0.5$ ps). These correspond to ideal internal quantum efficiency $IQE^{\infty} = 200\%$ (136% for $\tau_C^{red} = 0.5$ ps). We find that our proposed device is at ∼35% of the ideal performance (see Methods). If we include the metal absorption in the infinite device (∼28%, extrapolated from the ∼20% of the $L = 30$ μm device), we estimate $R_{I,ext}^{\infty}$ = 0.72 A/W and $R_{I,int}^{\infty}$ = 1.22 A/W for the ideal case of maximum field confinement (for $\tau_C^{red} = 0.5$ ps and $\rho_C = 1$ kΩ μm). Figure 8 puts all our findings into perspective, plotting the validation studies and predicted performance (proposed and ideal) in one graph. The excellent agreement between simulation and experiments (blue points in Figure 8) demonstrates the overall validity of our model.

We now consider other performance characteristics, i.e., sensitivity and speed. The sensitivity is quantified by the noise equivalent power (NEP), defined as NEP = $I_n/R_{I,ext}$, where I_n is the root-mean-square noise current density per hertz of BW in $A/Hz^{0.5}$.[75] At the optimal operation point with $R_{I,ext}$ = 0.6 A/W (assuming the faster cooling $\tau_C^{red} = 0.5$ ps at the contacts) and considering only thermal (Johnson) noise I_J (because of zero dark current) $I_n = I_J = \sqrt{(4k_BTR_D)} = 13$ $pA/Hz^{0.5}$[98] (see Methods), we estimate intrinsic NEP ∼ 22 $pW/Hz^{0.5}$. An interesting comparison is with the sensitivity of similar devices operated under a source−drain bias, V_{SD}, in which case dark current enters the shot noise. E.g., assuming V_{SD} = 0.5 V[31,45] and $R_D = 100$ Ω, we find I_D = 5 mA. Taking into consideration the shot noise component, the total noise current spectral density becomes $I_n = \sqrt{(I_J^2 + 2qI_D)} = 42$ $pA/Hz^{0.5}$ yielding, for $R_{I,ext}$ = 0.6 A/W, a NEP ∼70 $pW/Hz^{0.5}$ at P = 2.5 mW power consumption, more than triple the NEP of our unbiased device.

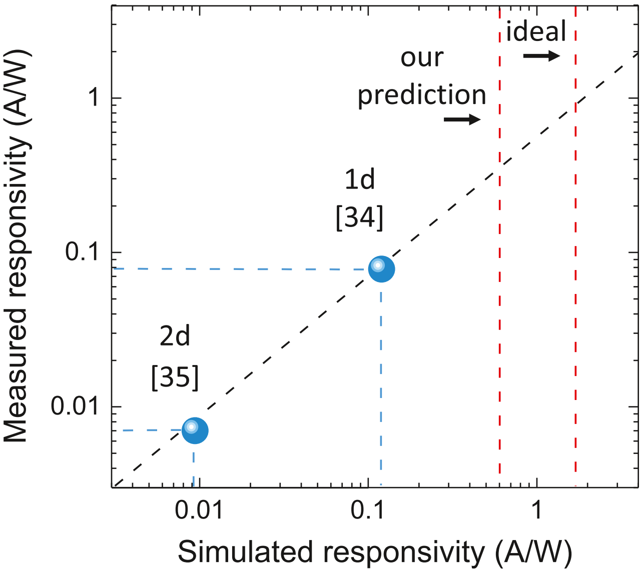

Figure 8. Simulated and measured $R_{I,ext}$ of the devices in refs 34 and 35 (blue points). The red lines mark the highest $R_{I,ext}$ prediction and the theoretical ideal internal $R_{I,int}^{\infty}$ for integrated asymmetric PTE PDs, including the 32% reduction at $\tau_C^{red} = 0.5$ ps.

We estimated the RC time constant of the device using the cutoff frequency $f_c = \{2\pi R_D\{[C_G^{-1} + C_q(E_F)^{-1}]^{-1} + C_{SD}\}\}^{-1}$, where C_G is the capacitance due to local gates, $C_q(E_F)$ is the SLG quantum capacitance,[114] and C_{SD} is the parasitic device capacitance. We assume C_{SD} = 20 fF as estimated in ref 35 for a similar device configuration. The gate capacitance is $C_G = \varepsilon\varepsilon_0 A/t$, where $\varepsilon_0 = 8.85 \times 10^{-12}$ F/m is the vacuum permittivity, $\varepsilon = 3.5$ is the hBN static dielectric constant,[115] t = 10 nm is the hBN thickness between SLG and substrate, and A is the gated area. $C_q(E_F) = e^2\nu(E_F)A$, where $\nu(E_F)$ is the SLG density of states at energy E_F (see Methods). For the fully gated device (both WG and side) $A = 30 \times 1.1$ μm^2, while for a

WG gate only, $A = 30 \times 0.35\ \mu m^2$ (assuming the optimal TE configuration at $L = 30\ \mu m$). For $R_D = 100\ \Omega$ and $E_F = -0.07$ eV, the fully gated and WG-gated configurations yield cutoff frequencies $f_c \sim 15$ GHz and ~ 34 GHz, respectively. If no gate is used, then f_c can reach up to ~ 80 GHz. We note that SLG τ_C ~2−4 ps,[46,82−89] and metal HC transfer/injection and cooling times of sub-ps[116] and ps,[108,117] result in a PTE-GPD intrinsic speed limit $\sim 1/\tau_C \sim 250$−500 GHz, much larger than the estimated RC device characteristic frequency (<100 GHz), making the latter a good estimate for the expected BW.[35]

■ CONCLUSIONS

Given the absence of band gap in SLG, an unbiased operation is preferred for GPDs to avoid large dark currents, shot noise, power consumption, and unwanted joule heating. Placing the metal contacts asymmetrically with respect to WGs promotes plasmonic-assisted light absorption in the SLG channel and allows for unbiased photodetection. Comprehensive optical-thermal-electrical modeling shows that, by tuning the SLG E_F and device architecture, high responsivity ($R_{I,ext} \sim 0.6$ A/W), sensitivity (NEP ~ 22 pW/Hz$^{0.5}$), and speed ($f \sim 80$ GHz) can be achieved for integrated photonics. This architecture can be further enhanced with local gates, yielding independent control over device resistance and responsivity, towards integrated balanced photodetection. Comparison with refs 34 and 35 validates our model assumptions and predictions. Together with the derived analytical expression for the ideal performance, this gives a perspective and outlook for integrated GPDs. E.g., in the ideal responsivity we assumed a fixed cooling time ($\tau_C = 3$ ps), carrier mobility ($\mu_q = 10{,}000$ cm^2/Vs), and contact resistance ($\rho_C = 1$ kΩ μm). Improving them will also increase responsivity (see Methods). Target areas of focus for improving performance should then be (i) increased SLG mobility (increased $R_{I,ext}$ and f), (ii) longer cooling time (increased $R_{I,ext}$), and (iii) lower contact resistance (increased $R_{I,ext}$ and f). Given our design's losses in scattering, transmission, and parasitic contact absorption, the focus should also be on (iv) improved plasmonic and/or metamaterial contact structures (less absorption losses). These pave the way toward $R_{I,ext} > 1$ A/W, NEP <10 pW/Hz$^{0.5}$, and f > 100 GHz in an unbiased integrated GPD.

■ METHODS

Optical Modeling. Optical calculations are performed with the Finite-difference time-domain method (FDTD, Lumerical[118]). The computational cell dimensions are $4 \times (L + 4) \times 5\ \mu m^3$, with perfectly matched layer (PML) conditions in all directions and with a 5 nm grid. The light source is the fundamental TE or TM optical mode of the Si WG at $\lambda = 1550$ nm. The dimensions of the device layers are given in Figure 1 and Table 1. The Au dielectric function is fitted with a Lumerical model.[119] hBN is anisotropic[120] with different permittivity in the in-plane (⊥) and out-of-plane (∥) directions. At $\lambda = 1550$ nm, its refractive index is[120] $n_\perp = 2.187$ and $n_\parallel = 1.715$. For SiO$_2$ and Si, we use $n_{Si} = 3.4757$[121] and $n_{SiO2} = 1.444$.[121] SLG is implemented as a 2d surface, with optical response modeled by the Kubo conductance[122] $\sigma = \sigma_{intra} + \sigma_{inter}$:

$$\sigma_{intra} = \frac{ie^2}{\pi\hbar^2\Omega}\int_0^\infty \varepsilon(\partial_\varepsilon f(-\varepsilon;\, \mu,\, T_e) - \partial_\varepsilon f(\varepsilon;\, \mu,\, T_e))d\varepsilon \tag{4}$$

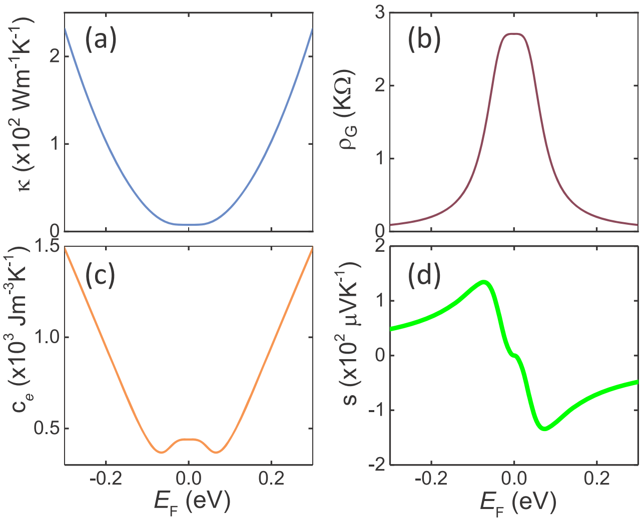

Figure 9. (a) Thermal conductivity, (b) specific resistivity, (c) thermal capacity, and (d) s as a function of SLG E_F for e/h mobility $\mu_q = 10{,}000$ cm^2/Vs, residual local charge fluctuation $n_0^* = 10^{11}$ cm^{-2}, and operation temperature 300 K.

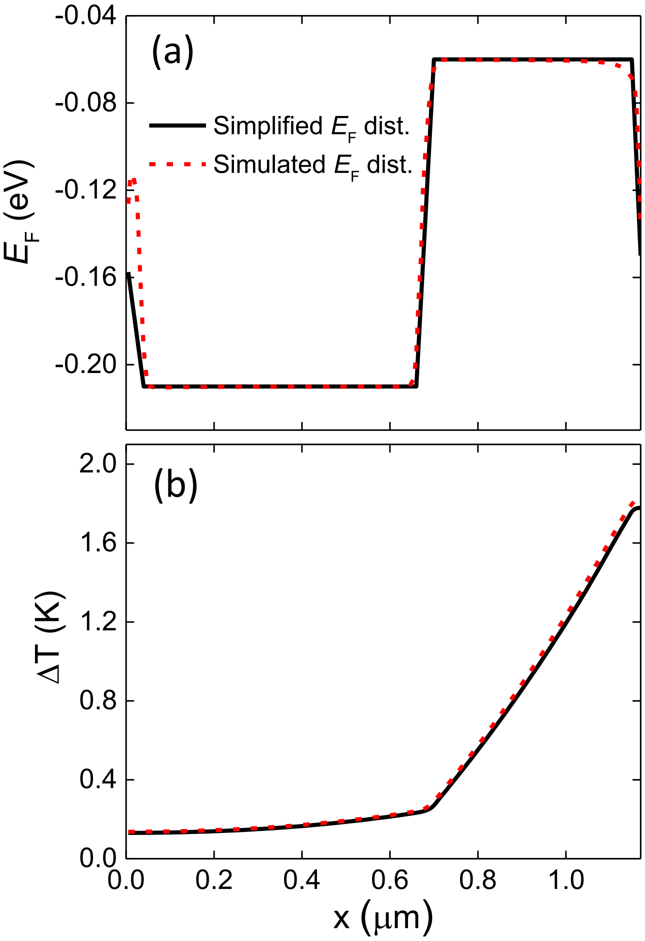

Figure 10. (a) E_F spatial distribution across the SLG channel for the double-gating with "WG" $E_F = -0.06$ eV and "side" $E_F = -0.21$ eV. (b) T_e increase distribution. The black solid lines correspond to results from the simplified E_F spatial distribution presented in the main text, while the red dot lines are the results using the E_F spatial distribution obtained by explicit electrostatic simulations.

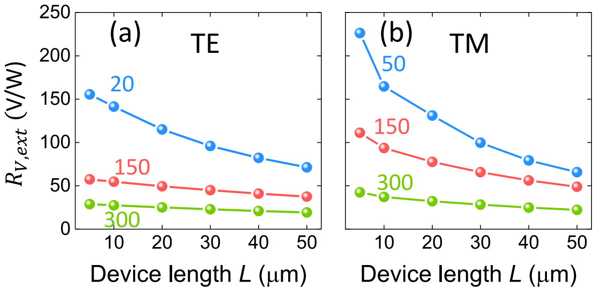

Figure 11. $R_{\mathrm{V,ext}}$ (V/W) for SLG with $E_F = -0.06$ eV at a 1d contact configuration, as a function of L (at fully embedded Si WG configuration and $w = 450$ nm). The numbers on the curves indicate different d. Panel (a) is for the TE, and panel (b) is for the TM mode.

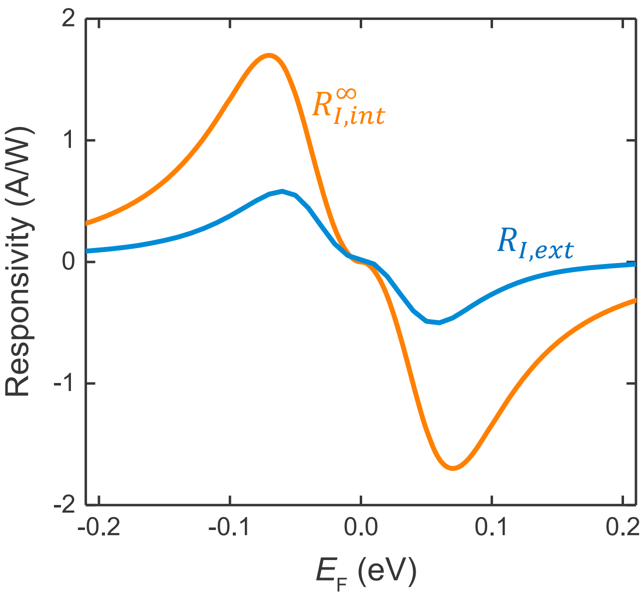

Figure 12. $R^{\infty}_{\mathrm{I,int}}$ and $R_{\mathrm{I,ext}}$ for the double-gating architecture as a function of SLG channel E_F and SLG "WG" E_F, respectively (in the latter case, the "side" E_F is set at $E_F^{\mathrm{side}} = -0.2$ eV). In both cases, we include the 32% reduction at $\tau_C^{\mathrm{red}} = 0.5$ ps.

$$\sigma_{\mathrm{inter}} = \frac{\mathrm{i}e^2\Omega}{\pi\hbar^2}\int_0^{\infty}\left(\frac{f(-\varepsilon;\,\mu,\,T_e) - f(\varepsilon;\,\mu,\,T_e)}{\Omega^2 - 4(\varepsilon/\hbar)^2}\right)\mathrm{d}\varepsilon \tag{5}$$

where $\Omega = \omega + \mathrm{i}\tau_{\mathrm{opt}}{}^{-1}$, τ_{opt} is the scattering time, $f(\varepsilon;\,\mu,\,T_e) = [\mathrm{e}^{(\varepsilon-\mu)/k_BT_e} + 1]^{-1}$ is the Fermi–Dirac distribution, and $\partial_\varepsilon \equiv \partial/\partial\varepsilon$. τ_{opt} is related to E_F and μ_q as $\tau_{\mathrm{opt}} = \mu_q|E_F|/ev_F{}^2$,[15] where $v_F = 10^6$ ms^{-1} is the SLG Fermi velocity. For $\mu_q = 10{,}000$ cm^2/Vs and $|E_F| = 0.2$ eV, we get $\tau_{\mathrm{opt}} = 200$ fs, used in eq 5.

Thermoelectric Modeling. We assume the quasi-cw case and solve the heat dissipation equation:[74]

$$-\nabla\cdot(\kappa\nabla T_e) = -\nabla\Pi\cdot j_q - \tau_C{}^{-1}c_e\Delta T + \alpha_{\mathrm{den}}P_{\mathrm{in}} \tag{6}$$

where κ is the electronic thermal conductivity, $\Pi = sT_e$ is the Peltier coefficient, $\boldsymbol{j}_q = -\sigma s\nabla T_e$ is the local thermoelectric current, σ is the electrical conductivity, c_e is the electronic heat capacity, $\Delta T = T_e - T_l$, α_{den} is the absorption density, and P_{in} is the incoming power. Note that in eq 6, $-\nabla\Pi\cdot \boldsymbol{j}_q = \boldsymbol{j}_q\cdot(\sigma^{-1}\boldsymbol{j}_q) - T_e\boldsymbol{j}_q\cdot\nabla s$, where the first term on the right is the Joule heating[123] and the second term includes both Peltier[124] (∇s at junction) and Thomson[125] (∇s in thermal gradient) effects. Due to the large SLG lattice heat capacity (compared to the electronic one),[90] we assume constant $T_l = 300$ K. The SLG parameters μ, σ, s, c_e, κ, and α_{den} are functions of E_F and T_e and are explicitly considered as such. The self-consistent solution of eq 6 provides the T_e distribution, from which the thermoelectric voltage is obtained:

$$V_{\mathrm{PTE}} = L^{-1}\int_0^L\int_0^W s\nabla T_e\,\mathrm{d}x\,\mathrm{d}y \tag{7}$$

The photocurrent is then $I_{\mathrm{PTE}} = V_{\mathrm{PTE}}/R_D$, where $R_D = R_G + 2R_C$ with $R_G = \int_0^W \sigma^{-1}(x)\mathrm{d}x$, $\sigma(x) = \int_0^L \sigma(x,\,y)\mathrm{d}y$ the SLG channel resistance and $R_C = \rho_C/L$ is the contact resistance, with ρ_C being the unit length contact resistance in units of Ω μm. Dividing by the input power, we get the external responsivities $R_{\mathrm{V,ext}} = V_{\mathrm{PTE}}/P_{\mathrm{in}}$ and $R_{\mathrm{I,ext}} = I_{\mathrm{PTE}}/P_{\mathrm{in}}$.

Zero bias PDs are limited by the Johnson noise,[98,126,127] when operating in frequencies above the corner frequency f_0 (defined as the frequency where the flicker ($1/f$) noise is equal to thermal or shot noise, typically ≤100 kHz for SLG devices[128]), assuming that they are perfectly shielded to minimize external noise and that have been impedance matched to minimize the amplifier noise. Also, possible contributions from generation–recombination noise, which occurs within the e–e scattering time scale (<50 fs[46,76,77]), have a small effect on SLG's local thermal equilibrium which gives rise to the PTE response and are not considered here. Thus the noise current (root-mean-square noise current density per Hz of BW in A/Hz$^{0.5}$) is $I_n = I_J = \sqrt{4k_BT/R_D}$,[98] where k_B is the Boltzmann constant and T is the operation temperature (300 K), and the intrinsic NEP = $I_n/R_{\mathrm{I,ext}}$ in units of W/Hz$^{0.5}$. We note that a linear photoresponse as a function of power is expected because the GPD operates in the weak heating regime ($\Delta T \ll T_{\mathrm{ambient}}$), where the electronic heat capacity can be considered constant.[34,37,76,98]

At finite T_e we obtain the chemical potential from the solution of[103] $\int_0^{\infty}\nu(\varepsilon)[f(\varepsilon;\,\mu,\,T_e) - f(\varepsilon;\,-\mu,\,T_e)]\mathrm{d}\varepsilon = E_F{}^2/\pi\hbar^2v_F{}^2$, where $\nu(\varepsilon) = 2|\varepsilon|/\pi\hbar^2v_F{}^2$ is the SLG density of states at energy ε. The other SLG electrical and thermal parameters in Figure 9 are calculated as follows: electrical conductivity $\sigma(\mu,\,T_e) = \int_{-\infty}^{\infty}\sigma(\varepsilon)(-\partial_\varepsilon f(\varepsilon;\,\mu,\,T_e))\mathrm{d}\varepsilon$, where $\sigma(\varepsilon) = q[\mu_q n(\varepsilon) + \bar{\mu}n^*(\varepsilon)]$, with $\mu_q = \mu_e/(\mu_h)$ for $\varepsilon > 0/(\varepsilon < 0)$ and $\bar{\mu} = (\mu_e + \mu_h)/2$. The effective residual local charge fluctuation at energy ε is $n^*(\varepsilon) = \sqrt{n(\varepsilon)^2 + n_0^{*2}} - n(\varepsilon)$, where $n(\varepsilon) = \varepsilon^2/\pi\hbar^2v_F{}^2$ is the SLG charge density at energy ε and n_0^* is the residual local charge fluctuation at the charge neutrality point.[129,130] From the Mott formula,[131] $s(\mu,\,T_e) = -(|e|T_e\sigma)^{-1}\int_{-\infty}^{\infty}(\varepsilon - \mu)\sigma(\varepsilon)(-\partial_\varepsilon f(\varepsilon;\,\mu,\,T_e))\mathrm{d}\varepsilon$. The electronic heat capacity[103] $c_e(\mu,\,T_e) = \partial_{T_e}\int_0^{\infty}\nu(\varepsilon)\varepsilon[f(\varepsilon;\,\mu,\,T_e) + f(\varepsilon;\,-\mu,\,T_e)]\mathrm{d}\varepsilon$, while thermal conductivity by the Wiedemann–Franz law[132] $\kappa(\mu,\,T_e) = L_0\sigma(\mu,\,T_e)T_e$, where $L_0 = 2.44 \times 10^{-8}$ W Ω K^{-2} is the Lorenz number.

Model Assumptions. The thermoelectric calculations assume SLG with $\mu_q = 10{,}000$ cm^2/Vs[75] for both e/h, residual local charge fluctuation $n_0^* = 10^{11}$ cm^{-2}[75] and $\tau_C = 3$ ps.[34,75] We use a typical value of unit length contact resistance $\rho_C = 1$ kΩ μm,[65,67,75] which for the 30 μm long device results in $2R_C = 66.7$ Ω. E_F of the SLG channel varies from −0.21 to 0.21 eV. The E_F pinning under the metal contacts is fixed at − 0.15 eV.[93] We introduce a narrow region extending 40 nm[34,73,98]

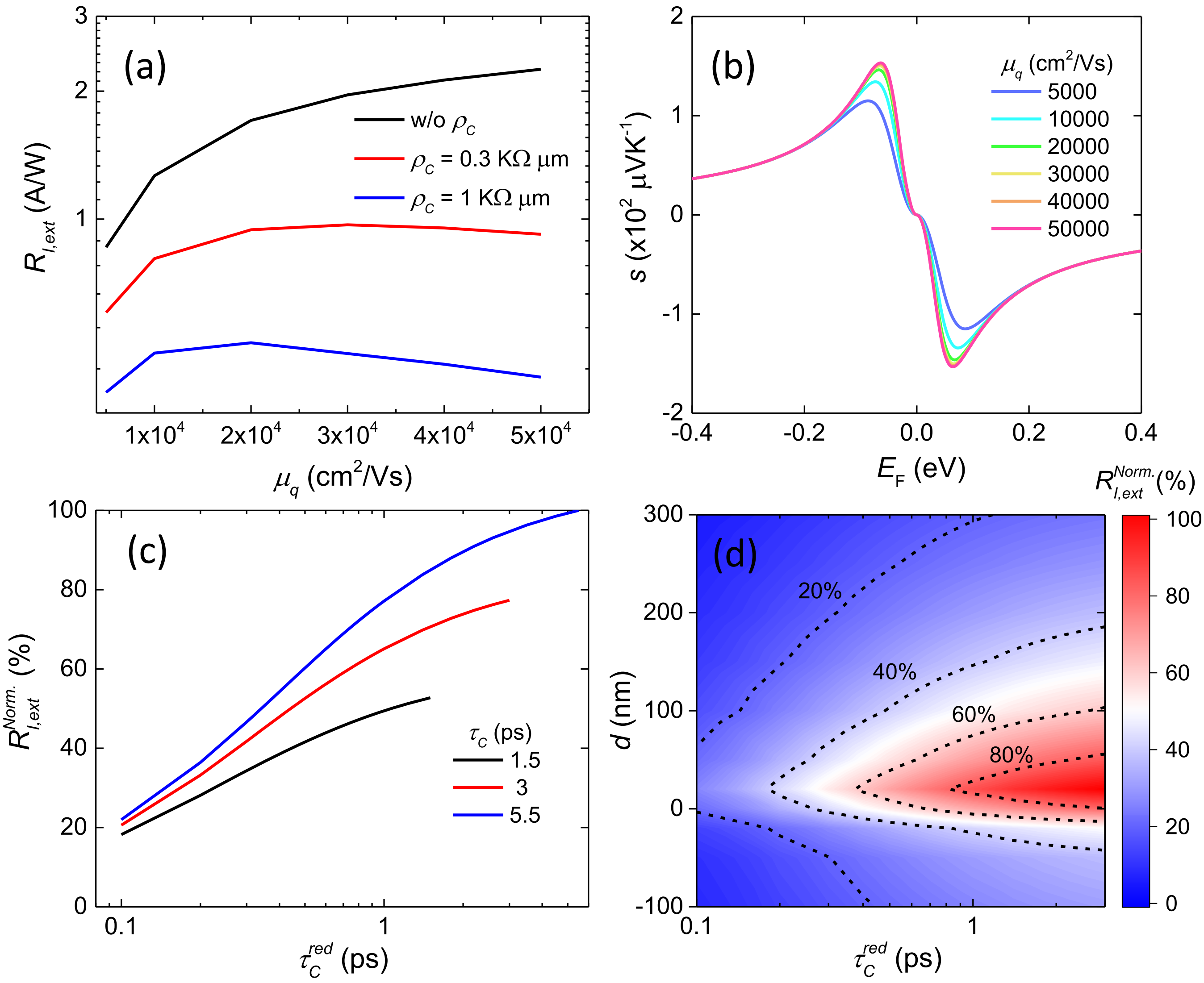

Figure 13. (a) $R_{I,ext}$ as a function of μ_q for three ρ_C for the optimal TE configuration of Figure 4 with τ_C = 3 ps and τ_C^{red} = 0.5 ps. (b) s as a function of E_F and μ_q. A linear relation between $1/n_0^*$ and μ_q is assumed as for ref 113. (c) $R_{I,ext}$ for E_F = −0.07 eV, as a function of τ_C and τ_C^{red} with ρ_C = 1 kΩ µm and μ_q = 10,000 cm^2/Vs. All $R_{I,ext}$ are normalized to $R_{I,ext}$ when $\tau_C^{red} = \tau_C$ = 5.5 ps. (d) $R_{I,ext}$ for E_F = −0.07 eV as a function of τ_C and d. All $R_{I,ext}$ normalized to that for $\tau_C^{red} = \tau_C$ = 3 ps and d = 20 nm. All calculations for the TE mode, L = 30 µm, w = 450 nm, 1d contact, and fully embedded Si WG.

from the contact edge into the SLG channel, within which the SLG E_F linearly scales back to the assumed channel E_F. For the double-gating architecture, the extension of the transition region in the contact close to the WG is bound by d. Almost identical results are obtained by assuming full electrostatic simulations, Figure 10. E_F can be tuned by V_G as $E_F = \mathrm{sgn}(V_G)\hbar v_F\sqrt{\pi\varepsilon_0\varepsilon_{hBN}|V_G|/et_{hBN}}$ where $\varepsilon_{hBN} = 3.5$[115] is the hBN spacer relative dielectric constant, and t_{hBN} = 10 nm is its thickness. The breakdown electric field for hBN is ~2 MV/cm for polycrystalline[115] and ~8 MV/cm for single crystal.[133] In our case, the V_G = 1.67 V required to dope SLG up to $|E_F|$ = 0.21 eV (the upper limit of our simulations) will produce an electric field ~1.67 MV/cm, well below breakdown.

Voltage Responsivity. We adopt the 1d contact configuration, E_F = −0.06 eV, and perform a series of optimization simulation runs, Figure 11, for both TE and TM polarizations to investigate the effect of device length on $R_{V,ext}$. The trends are very similar, with a monotonic $R_{V,ext}$ increase for shorter devices. This is due to the higher absorption density in the first µms of the device.

Ideal PTE Responsivity and Quantum Efficiency. To estimate the ideal PTE internal responsivity and quantum efficiency, we assume that absorption occurs only in SLG and close to one of the contacts (e.g., at x = 0) with a fixed τ_C. At steady state, for $x \neq 0$:

$$\kappa\nabla^2 T_e(x, y) - c_e\Delta T(x, y)\tau_C^{-1} = 0 \tag{8}$$

or

$$\nabla^2 T_e - \xi^{-2}\Delta T = 0 \tag{9}$$

where $\xi = \sqrt{\kappa\tau_C/c_e}$ is the cooling length. Assuming a decay length ψ due to absorption along the WG length L, the T_e profile can be written as:

$$\Delta T_e = \Delta T_e^0 e^{-y/\psi} e^{-x/\xi} \tag{10}$$

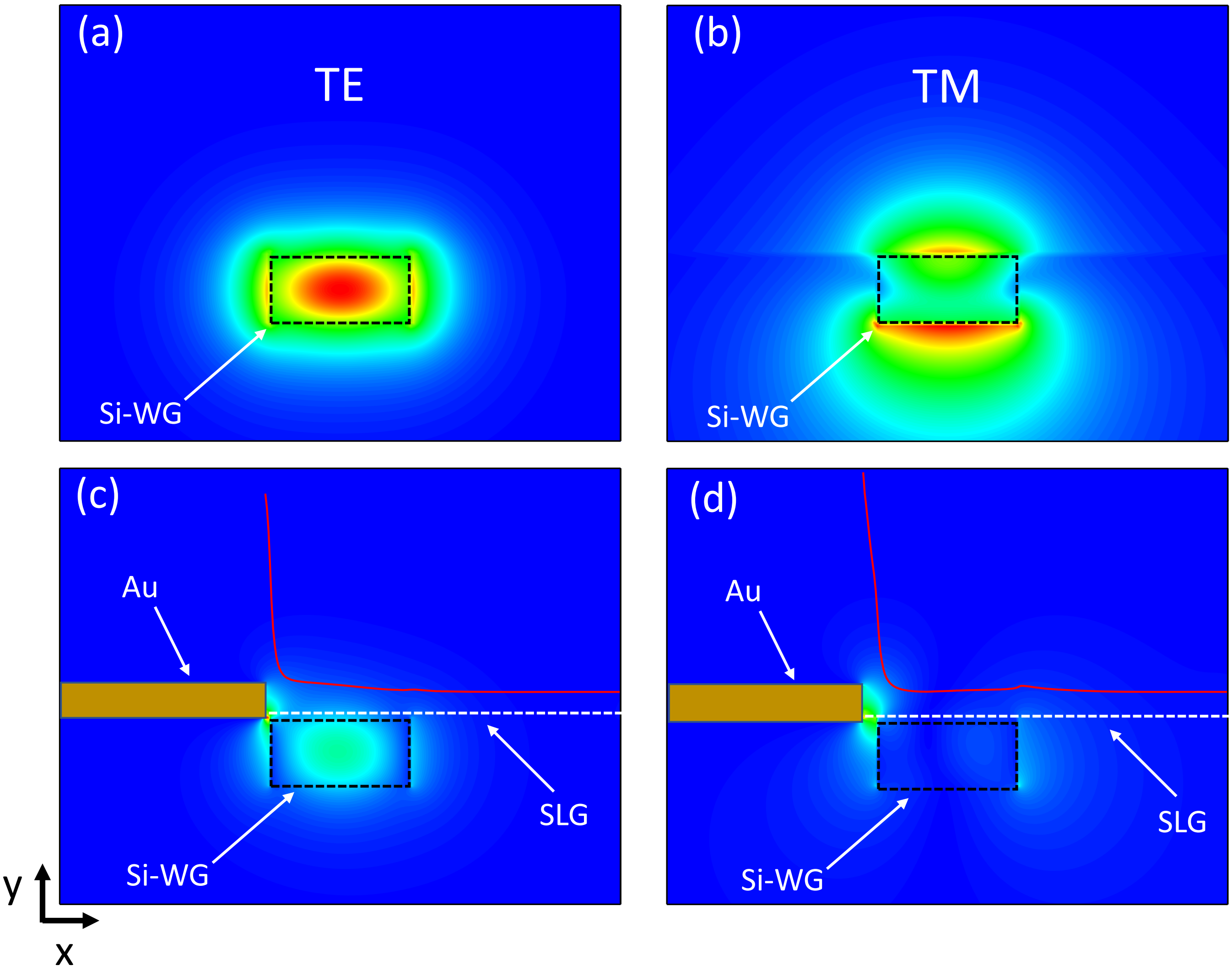

Figure 14. Si WG (w = 450 nm) optical mode field intensity profile for (a) TE and (b) TM polarization. $|E_x|$ field component of the hybrid optical-plasmonic mode for (c) TE (d = 20 nm) and (d) TM (d = 50 nm). The SLG absorption profile is shown as a red line in (c,d). Calculations are for 1d contact and fully embedded Si WG.

where ΔT_e^0 is the peak T_e rise, and the variables x (y) run perpendicular (along) the WG. ψ is used as a free parameter. The power lost to phonons in steady state is $c_e\tau_C^{-1}\Delta T_e(x,y)$. By integration, we find the total power P_{in}:

$$P_{in} = \int_0^\infty \int_0^\infty c_e\tau_C^{-1}\Delta T_e^0 e^{-y/\psi} e^{-x/\xi}\, dx\, dy = c_e\tau_C^{-1}\Delta T_e^0\psi\xi \tag{11}$$

The PTE voltage is found by integration over L (in the x direction we assume W is much larger than ξ):

$$\begin{aligned} V_{PTE} &= \frac{1}{L}\int_0^\infty \int_0^L s\Delta T_e^0 \frac{\partial}{\partial x}(e^{-y/\psi}e^{-x/\xi})dx\, dy \\ &= \frac{s\Delta T_e^0\psi}{L}(1 - e^{-L/\psi}) \end{aligned} \tag{12}$$

The voltage responsivity is then:

$$R_V = \frac{V_{PTE}}{P_{in}} = \frac{s\tau_C}{Lc_e\xi}(1 - e^{-L/\psi}) \tag{13}$$

where the term in the parenthesis accounts for light lost, that is, not absorbed, when L is comparable or smaller than ψ. By expanding ξ we find:

$$R_V = \frac{s}{L\beta}(1 - e^{-L/\psi}) \tag{14}$$

where $\beta = \sqrt{c_e\kappa/\tau_C}$ is a generalized heat exchange coefficient in W/mK. The max is at $L \to 0$, where the absorbed power density, thus T_e, is the highest:

$$R_V^0 = \frac{s}{\beta\psi} \tag{15}$$

To find R_I, we need the resistance as the sum of the SLG channel and contact contributions $R_D = R_G + 2R_C = (\rho'_G + 2\rho_C)/L$, with $\rho'_G = \rho_G W$, ρ_G is the graphene specific resistivity, and ρ_C the contact resistance [Ω m]. Setting the device conductance per unit length $g = (\rho'_G + 2\rho_C)^{-1}$ [Ω^{-1} m^{-1}] then:

$$R_I = \frac{R_V}{R_D} = \frac{gs\tau_C}{c_e\xi}(1 - e^{-L/\psi}) = \frac{gs}{\beta}(1 - e^{-L/\psi}) \tag{16}$$

R_I increases as we increase the device length (voltage drops but resistance drops too). For long devices (i.e., all light is absorbed in the SLG channel) we get the ideal internal responsivity:

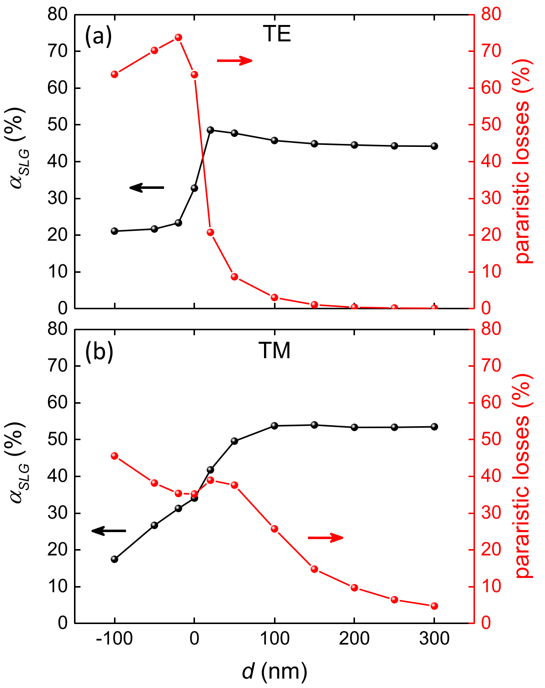

Figure 15. (a) SLG absorption, α_{SLG}, and parasitic losses (metal absorption and scattering) as a function of d for (a) TE and (b) TM modes. Calculations are for w = 450 nm, L = 30 μm, fully embedded Si WG, 1d contacts.

$$R_{\mathrm{I,int}}^{\infty} = \frac{gs}{\beta} \tag{17}$$

A comparison between $R_{I,\mathrm{int}}^{\infty}$ and $R_{I,\mathrm{ext}}$ of our proposed design is shown in Figure 12. The ideal internal quantum efficiency is:[30]

$$\mathrm{IQE}^{\infty} = \frac{\text{collected e} - \text{h pairs/s}}{\text{absorbed photons/s}} = \frac{I_{\mathrm{PTE}}/e}{P_{\mathrm{in}}/\hbar\omega} = \frac{gs}{\beta}\frac{hc}{\lambda e} \tag{18}$$

Effect of Mobility, Cooling Time, and Contact Resistance on Device Performance. We adopt the 1d contact configuration and perform simulation runs for the optimum TE configuration of Figure 4 to investigate the effect of μ_q, ρ_C, τ_C, and τ_C^{red} on device performance. μ_q covers 5000–50,000 cm^2/Vs, assuming a linear relation between $1/n_0^*$ and μ_q, according to ref 113. For τ_C, we use 1.5, 3, 5.5 ps, where the last value was measured in WSe$_2$-encapsulated SLG (WSe$_2$/SLG/WSe$_2$ stack with 124 nm total thickness, $\mu_q \geq 10{,}000$ cm^2/Vs).[89] As shown in Figure 13a, for zero contact resistance, higher μ_q and lower n_0^* result in monotonic increase of $R_{\mathrm{I,ext}}$. s saturates with improved SLG quality (i.e., for $\mu_q \geq 10{,}000$ cm^2/Vs, $n_0^* \leq 0.2 \times 10^{12}$ cm^{-2})[113,134] as the energy scale of n_0^* becomes comparable to k_BT,[134] Figure 13b. These $R_{\mathrm{I,ext}}$ results for $\rho_C = 0$ (channel limited) are consistent with eq 7, where $g = (\rho_G')^{-1} \propto \mu_q$ and $\beta \propto \sqrt{\kappa} \propto \sqrt{\mu_q}$, thus $R_I \propto s\sqrt{\mu_q}$. When a finite ρ_C is introduced, the trend changes, and the peak $R_{\mathrm{I,ext}}$ is observed for lower μ_q as ρ_C increases. In the limit where the total device resistance is dominated by the contact resistance $g \sim 1/2\rho_C$ (contact limited), the dominant contribution comes from the increased thermal conductivity. Thus $R_I \propto s/\sqrt{\mu_q}$, i.e., reduced for increasing μ_q.

An increased cooling time improves $R_{\mathrm{I,ext}}$. As shown in Figure 13c, for $\tau_C^{\mathrm{red}} = \tau_C$, 90% and 30% increase in $R_{\mathrm{I,ext}}$ is achieved for τ_C = 5.5 ps compared to 1.5 and 3 ps, respectively, consistent with what is expected from our analytical theory $R_I \propto 1/\beta \propto \sqrt{\tau_C}$. When we introduce faster cooling at/under the metal contact ($\tau_C^{\mathrm{red}} < \tau_C$), the performance differences diminish and converge to a common value. The faster cooling at/under the metal contacts does not alter the optimum device configuration. As shown in Figure 13d, the optimal d is unaffected by τ_C^{red}.

Trade-off between Field Enhancement and Plasmonic Losses. As shown in Figures 2 and 14, the plasmonic excitation in the metal contacts results (as we reduce d) in field redistribution, enhanced field confinement, and increase of the SLG absorption density near the metal contact.

This increased absorption density is translated in larger T_e and $R_{\mathrm{I,ext}}$ with optimum d = 20 nm for TE and 50 nm for TM. To understand this behavior, we plot in Figure 15 the SLG absorption and the parasitic losses (metal absorption and scattering) as a function of d for both TE and TM modes. As d decreases to its optimal value, the gain from the increased plasmonic field confinement of the hybridized optical-SPP mode dominates the parasitic losses, yielding an enhanced T_e gradient and $R_{\mathrm{I,ext}}$. Below the optimal d, metal losses and scattering increase at the expense of SLG absorption, resulting in reduced $R_{\mathrm{I,ext}}$, Figure 4.

Effect of Metal HC Injection/Transfer on Device Performance. As d reduces and the absorption in the metal contact increases due to the excitation of SPP modes (see Figure 15), photoexcited HC in the metal can in principle inject[91] into the SLG channel and affect the responsivity.[92] To quantify this, we estimate an upper limit of the metal HC contribution to the photocurrent using the optimized device (TE polarization, d = 20 nm) where we find a metal absorption $\alpha_M \sim 20\%$ (see Figure 15a). If we assume all metal HCs with velocity normal to the interface to be injected and contribute to the photocurrent (i.e., 1/4 of them), then the metal HC current contribution is $R_{\mathrm{I,HC}} = \alpha_M \times 0.25 \times \mathrm{e}/\hbar\omega = 0.0625$ A/W. This corresponds to ~ 10% of the maximum calculated $R_{\mathrm{I,ext}}$ = 0.6 A/W. Given this upper limit, we expect the metal plasmonic HC effects to be a small correction.

■ AUTHOR INFORMATION

Corresponding Author

Elefterios Lidorikis – *Department of Materials Science and Engineering, University of Ioannina, Ioannina 45110, Greece; University Research Center of Ioannina (URCI), Institute of Materials Science and Computing, Ioannina 45110, Greece;* orcid.org/0000-0002-9552-9366; Email: elidorik@uoi.gr

Authors

Ioannis Vangelidis – *Department of Materials Science and Engineering, University of Ioannina, Ioannina 45110, Greece;* orcid.org/0000-0002-7488-4166

Dimitris V. Bellas – *Department of Materials Science and Engineering, University of Ioannina, Ioannina 45110, Greece; Department of Informatics, Center for Interdisciplinary Research and Innovation, Aristotle University of Thessaloniki, Thessaloniki 57001, Greece*

Stephan Suckow – *AMO GmbH, Advanced Microelectronic Center Aachen (AMICA), Aachen 52074, Germany;* orcid.org/0000-0002-1116-169X

George Dabos – *Department of Informatics, Center for Interdisciplinary Research and Innovation, Aristotle University of Thessaloniki, Thessaloniki 57001, Greece*

Sebastián Castilla – *ICFO - Institut de Ciències Fotòniques, The Barcelona Institute of Science and Technology, Barcelona 08860, Spain;* orcid.org/0000-0002-8899-0525

Frank H. L. Koppens – *ICFO - Institut de Ciències Fotòniques, The Barcelona Institute of Science and Technology, Barcelona 08860, Spain; ICREA - Institució Catalana de Recerca i Estudis Avançats, Barcelona 08010, Spain;* orcid.org/0000-0001-9764-6120

Andrea C. Ferrari – *Cambridge Graphene Centre, University of Cambridge, Cambridge CB3 0FA, U.K.;* orcid.org/0000-0003-0907-9993

Nikos Pleros – *Department of Informatics, Center for Interdisciplinary Research and Innovation, Aristotle University of Thessaloniki, Thessaloniki 57001, Greece*

Complete contact information is available at: https://pubs.acs.org/10.1021/acsphotonics.2c00100

Funding

We acknowledge funding from the Graphene and Quantum Flagships, EU Grant Plasmoniac, ERC grant Hetero2D, EPSRC grants EP/L016087/1, EP/K01711X/1, EP/K017144/1, EP/N010345/1, and DSTL. For the purpose of open access, the authors applied a Creative Commons Attribution (CC BY) license to any Author Accepted Manuscript version arising from this submission.

Notes

The authors declare no competing financial interest.

REFERENCES

(1) Helkey, R.; Saleh, A. A. M.; Buckwalter, J.; Bowers, J. E. High-Performance Photonic Integrated Circuits on Silicon. *IEEE J. Sel. Top. Quantum Electron.* **2019**, *25*, 1–15.

(2) Fathololoumi, S.; et al. 1.6 Tbps Silicon Photonics Integrated Circuit and 800 Gbps Photonic Engine for Switch Co-Packaging Demonstration. *J. Lightwave Technol.* **2021**, *39*, 1155–1161.

(3) Pitris, S.; Mitsolidou, C.; Moralis-Pegios, M.; Fotiadis, K.; Ban, Y.; De Heyn, P.; Van Campenhout, J.; Lambrecht, J.; Ramon, H.; Yin, X.; Bauwelinck, J.; Pleros, N.; Alexoudi, T. 400 Gb/s Silicon Photonic Transmitter and Routing WDM Technologies for Glueless 8-Socket Chip-to-Chip Interconnects. *J. Lightwave Technol.* **2020**, *38*, 3366–3375.

(4) Minzioni, P.; et al. Roadmap on all-optical processing. *J. Opt.* **2019**, *21*, 063001.

(5) Alexoudi, T.; Kanellos, G. T.; Pleros, N. Optical RAM and integrated optical memories: a survey. *Light: Sci. Appl.* **2020**, *9*, 91.

(6) Totović, A. R.; Dabos, G.; Passalis, N.; Tefas, A.; Pleros, N. Femtojoule per MAC Neuromorphic Photonics: An Energy and Technology Roadmap. *IEEE J. Sel. Top. Quantum Electron.* **2020**, *26*, 1–15.

(7) Shen, Y.; Harris, N. C.; Skirlo, S.; Prabhu, M.; Baehr-Jones, T.; Hochberg, M.; Sun, X.; Zhao, S.; Larochelle, H.; Englund, D.; Soljačić, M. Deep learning with coherent nanophotonic circuits. *Nat. Photonics* **2017**, *11*, 441–446.

(8) Shastri, B. J.; Tait, A. N.; Ferreira de Lima, T.; Pernice, W. H. P.; Bhaskaran, H.; Wright, C. D.; Prucnal, P. R. Photonics for artificial intelligence and neuromorphic computing. *Nat. Photonics* **2021**, *15*, 102–114.

(9) Patrizio, A. Ethernet Consortium Releases 800GbE Spec. https://www.networkworld.com/article/3538529/ethernet-consortium-releases-800gbespec.html (accessed Jan 12, 2021).

(10) Akinwande, D.; Huyghebaert, C.; Wang, C.-H.; Serna, M. I.; Goossens, S.; Li, L.-J.; Wong, H.-S. P.; Koppens, F. H. L. Graphene and two-dimensional materials for silicon technology. *Nature* **2019**, *573*, 507–518.

(11) Salamin, Y.; Ma, P.; Baeuerle, B.; Emboras, A.; Fedoryshyn, Y.; Heni, W.; Cheng, B.; Josten, A.; Leuthold, J. 100 GHz Plasmonic Photodetector. *ACS Photonics* **2018**, *5*, 3291–3297.

(12) Thomson, D.; et al. Roadmap on silicon photonics. *J. Opt.* **2016**, *18*, 073003.

(13) Vivien, L.; Osmond, J.; Fédéli, J.-M.; Marris-Morini, D.; Crozat, P.; Damlencourt, J.-F.; Cassan, E.; Lecunff, Y.; Laval, S. 42 GHz pin Germanium photodetector integrated in a silicon-on-insulator waveguide. *Opt. Express* **2009**, *17*, 6252–6257.

(14) Stojanović, V.; Ram, R. J.; Popović, M.; Lin, S.; Moazeni, S.; Wade, M.; Sun, C.; Alloatti, L.; Atabaki, A.; Pavanello, F.; Mehta, N.; Bhargava, P. Monolithic silicon-photonic platforms in state-of-the-art CMOS SOI processes [Invited]. *Opt. Express* **2018**, *26*, 13106–13121.

(15) Romagnoli, M.; Sorianello, V.; Midrio, M.; Koppens, F. H. L.; Huyghebaert, C.; Neumaier, D.; Galli, P.; Templ, W.; D'Errico, A.; Ferrari, A. C. Graphene-based integrated photonics for next-generation datacom and telecom. *Nat. Rev. Mater.* **2018**, *3*, 392–414.

(16) Hobbs, P. C. D. Ultrasensitive laser measurements without tears. *Appl. Opt.* **1997**, *36*, 903–920.

(17) Runge, P.; Zhou, G.; Beckerwerth, T.; Ganzer, F.; Keyvaninia, S.; Seifert, S.; Ebert, W.; Mutschall, S.; Seeger, A.; Schell, M. Waveguide Integrated Balanced Photodetectors for Coherent Receivers. *IEEE J. Sel. Top. Quantum Electron.* **2018**, *24*, 1–7.

(18) Hai, M. S.; Sakib, M. N.; Liboiron-Ladouceur, O. A 16 GHz silicon-based monolithic balanced photodetector with on-chip capacitors for 25 Gbaud front-end receivers. *Opt. Express* **2013**, *21*, 32680–32689.

(19) Painchaud, Y.; Poulin, M.; Morin, M.; Têtu, M. Performance of balanced detection in a coherent receiver. *Opt. Express* **2009**, *17*, 3659–3672.

(20) Wang, J.; Lee, S. Ge-photodetectors for Si-based optoelectronic integration. *Sensors* **2011**, *11*, 696–718.

(21) Michel, J.; Liu, J.; Kimerling, L. C. High-performance Ge-on-Si photodetectors. *Nat. Photonics* **2010**, *4*, 527–534.

(22) Liang, D.; Roelkens, G.; Baets, R.; Bowers, J. Hybrid Integrated Platforms for Silicon Photonics. *Materials* **2010**, *3*, 1782–1802.

(23) Beling, A.; Campbell, J. C. InP-Based High-Speed Photodetectors. *J. Lightwave Technol.* **2009**, *27*, 343–355.

(24) Chrostowski, L.; Hochberg, M. *Silicon Photonics Design: From Devices to Systems*; Cambridge University Press, 2015.

(25) Ye, H.; Yu, J. Germanium epitaxy on silicon. *Sci. Technol. Adv. Mater.* **2014**, *15*, 024601.

(26) Novack, A.; Gould, M.; Yang, Y.; Xuan, Z.; Streshinsky, M.; Liu, Y.; Capellini, G.; Lim, A. E.-J.; Lo, G.-Q.; Baehr-Jones, T.; Hochberg, M. Germanium photodetector with 60 GHz bandwidth using inductive gain peaking. *Opt. Express* **2013**, *21*, 28387–28393.

(27) Absil, P. P.; Verheyen, P.; De Heyn, P.; Pantouvaki, M.; Lepage, G.; De Coster, J.; Van Campenhout, J. Silicon photonics integrated circuits: a manufacturing platform for high density, low power optical I/O's. *Opt. Express* **2015**, *23*, 9369–9378.

(28) Ferrari, A. C.; et al. Science and technology roadmap for graphene, related two-dimensional crystals, and hybrid systems. *Nanoscale* **2015**, *7*, 4598–4810.

(29) Bonaccorso, F.; Sun, Z.; Hasan, T.; Ferrari, A. C. Graphene photonics and optoelectronics. *Nat. Photonics* **2010**, *4*, 611–622.

(30) Koppens, F. H. L.; Mueller, T.; Avouris, P.; Ferrari, A. C.; Vitiello, M. S.; Polini, M. Photodetectors based on graphene, other two-dimensional materials and hybrid systems. *Nat. Nanotechnol.* **2014**, *9*, 780–793.

(31) Ma, P.; Salamin, Y.; Baeuerle, B.; Josten, A.; Heni, W.; Emboras, A.; Leuthold, J. Plasmonically Enhanced Graphene Photodetector Featuring 100 Gbit/s Data Reception, High Responsivity, and Compact Size. *ACS Photonics* **2019**, *6*, 154–161.

(32) Gao, Y.; Zhou, G.; Zhao, N.; Tsang, H. K.; Shu, C. High-performance chemical vapor deposited graphene-on-silicon nitride waveguide photodetectors. *Opt. Lett.* **2018**, *43*, 1399–1402.

(33) Gan, X.; Shiue, R.-J.; Gao, Y.; Meric, I.; Heinz, T. F.; Shepard, K.; Hone, J.; Assefa, S.; Englund, D. Chip-integrated ultrafast graphene photodetector with high responsivity. *Nat. Photonics* **2013**, *7*, 883−887.

(34) Shiue, R.-J.; Gao, Y.; Wang, Y.; Peng, C.; Robertson, A. D.; Efetov, D. K.; Assefa, S.; Koppens, F. H. L.; Hone, J.; Englund, D. High-Responsivity Graphene-Boron Nitride Photodetector and Autocorrelator in a Silicon Photonic Integrated Circuit. *Nano Lett.* **2015**, *15*, 7288−7293.

(35) Schall, D.; Neumaier, D.; Mohsin, M.; Chmielak, B.; Bolten, J.; Porschatis, C.; Prinzen, A.; Matheisen, C.; Kuebart, W.; Junginger, B.; Templ, W.; Giesecke, A. L.; Kurz, H. 50 GBit/s Photodetectors Based on Wafer-Scale Graphene for Integrated Silicon Photonic Communication Systems. *ACS Photonics* **2014**, *1*, 781−784.

(36) Schuler, S.; Schall, D.; Neumaier, D.; Dobusch, L.; Bethge, O.; Schwarz, B.; Krall, M.; Mueller, T. Controlled Generation of a p-n Junction in a Waveguide Integrated Graphene Photodetector. *Nano Lett.* **2016**, *16*, 7107−7112.

(37) Muench, J. E.; et al. Waveguide-Integrated, Plasmonic Enhanced Graphene Photodetectors. *Nano Lett.* **2019**, *19*, 7632−7644.

(38) Mišeikis, V.; et al. Ultrafast, Zero-Bias, Graphene Photodetectors with Polymeric Gate Dielectric on Passive Photonic Waveguides. *ACS Nano* **2020**, *14*, 11190−11204.

(39) Marconi, S.; Giambra, M. A.; Montanaro, A.; Mišeikis, V.; Soresi, S.; Tirelli, S.; Galli, P.; Buchali, F.; Templ, W.; Coletti, C.; Sorianello, V.; Romagnoli, M. Photo thermal effect graphene detector featuring 105 Gbit s−1 NRZ and 120 Gbit s−1 PAM4 direct detection. *Nat. Commun.* **2021**, *12*, 806.

(40) Schuler, S.; Schall, D.; Neumaier, D.; Schwarz, B.; Watanabe, K.; Taniguchi, T.; Mueller, T. Graphene Photodetector Integrated on a Photonic Crystal Defect Waveguide. *ACS Photonics* **2018**, *5*, 4758−4763.

(41) Ding, Y.; Cheng, Z.; Zhu, X.; Yvind, K.; Dong, J.; Galili, M.; Hu, H.; Mortensen, N. A.; Xiao, S.; Oxenløwe, L. K. Ultra-compact integrated graphene plasmonic photodetector with bandwidth above 110 GHz. *Nanophotonics* **2020**, *9*, 317−325.

(42) Ma, Z.; Kikunaga, K.; Wang, H.; Sun, S.; Amin, R.; Maiti, R.; Tahersima, M. H.; Dalir, H.; Miscuglio, M.; Sorger, V. J. Compact Graphene Plasmonic Slot Photodetector on Silicon-on-Insulator with High Responsivity. *ACS Photonics* **2020**, *7*, 932−940.

(43) Goykhman, I.; Sassi, U.; Desiatov, B.; Mazurski, N.; Milana, S.; de Fazio, D.; Eiden, A.; Khurgin, J.; Shappir, J.; Levy, U.; Ferrari, A. C. On-Chip Integrated, Silicon-Graphene Plasmonic Schottky Photodetector with High Responsivity and Avalanche Photogain. *Nano Lett.* **2016**, *16*, 3005−3013.

(44) Schuler, S.; Muench, J. E.; Ruocco, A.; Balci, O.; Thourhout, D. v.; Sorianello, V.; Romagnoli, M.; Watanabe, K.; Taniguchi, T.; Goykhman, I.; Ferrari, A. C.; Mueller, T. High-responsivity graphene photodetectors integrated on silicon microring resonators. *Nat. Commun.* **2021**, *12*, 3733.

(45) Schall, D.; Pallecchi, E.; Ducournau, G.; Avramovic, V.; Otto, M.; Neumaier, D. *Record High Bandwidth Integrated Graphene Photodetectors for Communication beyond 180 Gb/s. 2018 Optical Fiber Communications Conference and Exposition*; OFC, 2018; pp 1−3.

(46) Brida, D.; Tomadin, A.; Manzoni, C.; Kim, Y. J.; Lombardo, A.; Milana, S.; Nair, R. R.; Novoselov, K. S.; Ferrari, A. C.; Cerullo, G.; Polini, M. Ultrafast collinear scattering and carrier multiplication in graphene. *Nat. Commun.* **2013**, *4*, 1987.

(47) Mayorov, A. S.; Elias, D. C.; Mucha-Kruczynski, M.; Gorbachev, R. V.; Tudorovskiy, T.; Zhukov, A.; Morozov, S. V.; Katsnelson, M. I.; Geim, A. K.; Novoselov, K. S. Interaction-Driven Spectrum Reconstruction in Bilayer Graphene. *Science* **2011**, *333*, 860−863.

(48) Bolotin, K. I.; Sikes, K. J.; Jiang, Z.; Klima, M.; Fudenberg, G.; Hone, J.; Kim, P.; Stormer, H. L. Ultrahigh electron mobility in suspended graphene. *Solid State Commun.* **2008**, *146*, 351−355.

(49) Dorgan, V. E.; Bae, M.-H.; Pop, E. Mobility and saturation velocity in graphene on SiO2. *Appl. Phys. Lett.* **2010**, *97*, 082112.

(50) De Fazio, D.; Purdie, D. G.; Ott, A. K.; Braeuninger-Weimer, P.; Khodkov, T.; Goossens, S.; Taniguchi, T.; Watanabe, K.; Livreri, P.; Koppens, F. H. L.; Hofmann, S.; Goykhman, I.; Ferrari, A. C.; Lombardo, A. High-Mobility, Wet-Transferred Graphene Grown by Chemical Vapor Deposition. *ACS Nano* **2019**, *13*, 8926−8935.

(51) Purdie, D. G.; Pugno, N. M.; Taniguchi, T.; Watanabe, K.; Ferrari, A. C.; Lombardo, A. Cleaning interfaces in layered materials heterostructures. *Nat. Commun.* **2018**, *9*, 5387.

(52) Pospischil, A.; Humer, M.; Furchi, M. M.; Bachmann, D.; Guider, R.; Fromherz, T.; Mueller, T. CMOS-compatible graphene photodetector covering all optical communication bands. *Nat. Photonics* **2013**, *7*, 892−896.

(53) Giambra, M. A.; Mišeikis, V.; Pezzini, S.; Marconi, S.; Montanaro, A.; Fabbri, F.; Sorianello, V.; Ferrari, A. C.; Coletti, C.; Romagnoli, M. Wafer-Scale Integration of Graphene-Based Photonic Devices. *ACS Nano* **2021**, *15*, 3171−3187.

(54) Das, A.; Pisana, S.; Chakraborty, B.; Piscanec, S.; Saha, S. K.; Waghmare, U. V.; Novoselov, K. S.; Krishnamurthy, H. R.; Geim, A. K.; Ferrari, A. C.; Sood, A. K. Monitoring dopants by Raman scattering in an electrochemically top-gated graphene transistor. *Nat. Nanotechnol.* **2008**, *3*, 210−215.

(55) Pisana, S.; Lazzeri, M.; Casiraghi, C.; Novoselov, K. S.; Geim, A. K.; Ferrari, A. C.; Mauri, F. Breakdown of the adiabatic Born-Oppenheimer approximation in graphene. *Nat. Mater.* **2007**, *6*, 198−201.

(56) Li, Z. Q.; Henriksen, E. A.; Jiang, Z.; Hao, Z.; Martin, M. C.; Kim, P.; Stormer, H. L.; Basov, D. N. Dirac charge dynamics in graphene by infrared spectroscopy. *Nat. Phys.* **2008**, *4*, 532−535.

(57) Wang, F.; Zhang, Y.; Tian, C.; Girit, C.; Zettl, A.; Crommie, M.; Shen, Y. R. Gate-Variable Optical Transitions in Graphene. *Science* **2008**, *320*, 206−209.

(58) Nair, R. R.; Blake, P.; Grigorenko, A. N.; Novoselov, K. S.; Booth, T. J.; Stauber, T.; Peres, N. M. R.; Geim, A. K. Fine Structure Constant Defines Visual Transparency of Graphene. *Science* **2008**, *320*, 1308.

(59) Dawlaty, J. M.; Shivaraman, S.; Strait, J.; George, P.; Chandrashekhar, M.; Rana, F.; Spencer, M. G.; Veksler, D.; Chen, Y. Measurement of the optical absorption spectra of epitaxial graphene from terahertz to visible. *Appl. Phys. Lett.* **2008**, *93*, 131905.

(60) Freitag, M.; Low, T.; Xia, F.; Avouris, P. Photoconductivity of biased graphene. *Nat. Photonics* **2013**, *7*, 53−59.

(61) Castro Neto, A. H.; Guinea, F.; Peres, N. M. R.; Novoselov, K. S.; Geim, A. K. The electronic properties of graphene. *Rev. Mod. Phys.* **2009**, *81*, 109−162.

(62) Gabor, N. M.; Song, J. C. W.; Ma, Q.; Nair, N. L.; Taychatanapat, T.; Watanabe, K.; Taniguchi, T.; Levitov, L. S.; Jarillo-Herrero, P. Hot Carrier-Assisted Intrinsic Photoresponse in Graphene. *Science* **2011**, *334*, 648−652.

(63) Echtermeyer, T. J.; Milana, S.; Sassi, U.; Eiden, A.; Wu, M.; Lidorikis, E.; Ferrari, A. C. Surface Plasmon Polariton Graphene Photodetectors. *Nano Lett.* **2016**, *16*, 8−20.

(64) Dean, C. R.; Young, A. F.; Meric, I.; Lee, C.; Wang, L.; Sorgenfrei, S.; Watanabe, K.; Taniguchi, T.; Kim, P.; Shepard, K. L.; Hone, J. Boron nitride substrates for high-quality graphene electronics. *Nat. Nanotechnol.* **2010**, *5*, 722−726.

(65) Wang, L.; Meric, I.; Huang, P. Y.; Gao, Q.; Gao, Y.; Tran, H.; Taniguchi, T.; Watanabe, K.; Campos, L. M.; Muller, D. A.; Guo, J.; Kim, P.; Hone, J.; Shepard, K. L.; Dean, C. R. One-Dimensional Electrical Contact to a Two-Dimensional Material. *Science* **2013**, *342*, 614−617.

(66) Giubileo, F.; Di Bartolomeo, A. The role of contact resistance in graphene field-effect devices. *Prog. Surf. Sci.* **2017**, *92*, 143−175.

(67) Xia, F.; Perebeinos, V.; Lin, Y.-m.; Wu, Y.; Avouris, P. The origins and limits of metal-graphene junction resistance. *Nat. Nanotechnol.* **2011**, *6*, 179−184.

(68) Park, J.; Ahn, Y. H.; Ruiz-Vargas, C. Imaging of Photocurrent Generation and Collection in Single-Layer Graphene. *Nano Lett.* **2009**, *9*, 1742−1746.

(69) Echtermeyer, T. J.; Nene, P. S.; Trushin, M.; Gorbachev, R. V.; Eiden, A. L.; Milana, S.; Sun, Z.; Schliemann, J.; Lidorikis, E.; Novoselov, K. S.; Ferrari, A. C. Photothermoelectric and Photoelectric Contributions to Light Detection in Metal-Graphene-Metal Photodetectors. *Nano Lett.* **2014**, *14*, 3733−3742.

(70) Lee, E. J. H.; Balasubramanian, K.; Weitz, R. T.; Burghard, M.; Kern, K. Contact and edge effects in graphene devices. *Nat. Nanotechnol.* **2008**, *3*, 486−490.

(71) Mueller, T.; Xia, F.; Freitag, M.; Tsang, J.; Avouris, P. Role of contacts in graphene transistors: A scanning photocurrent study. *Phys. Rev. B* **2009**, *79*, 245430.

(72) Tielrooij, K. J.; Massicotte, M.; Piatkowski, L.; Woessner, A.; Ma, Q.; Jarillo-Herrero, P.; Hulst, N. F. v.; Koppens, F. H. L. Hot-carrier photocurrent effects at graphene-metal interfaces. *J. Phys.: Condens. Matter* **2015**, *27*, 164207.

(73) Mueller, T.; Xia, F.; Avouris, P. Graphene photodetectors for high-speed optical communications. *Nat. Photonics* **2010**, *4*, 297−301.

(74) Song, J. C. W.; Rudner, M. S.; Marcus, C. M.; Levitov, L. S. Hot Carrier Transport and Photocurrent Response in Graphene. *Nano Lett.* **2011**, *11*, 4688−4692.

(75) Castilla, S.; et al. Plasmonic antenna coupling to hyperbolic phonon-polaritons for sensitive and fast mid-infrared photodetection with graphene. *Nat. Commun.* **2020**, *11*, 4872.

(76) Tielrooij, K. J.; Piatkowski, L.; Massicotte, M.; Woessner, A.; Ma, Q.; Lee, Y.; Myhro, K. S.; Lau, C. N.; Jarillo-Herrero, P.; van Hulst, N. F.; Koppens, F. H. L. Generation of photovoltage in graphene on a femtosecond timescale through efficient carrier heating. *Nat. Nanotechnol.* **2015**, *10*, 437−443.

(77) Massicotte, M.; Soavi, G.; Principi, A.; Tielrooij, K.-J. Hot carriers in graphene - fundamentals and applications. *Nanoscale* **2021**, *13*, 8376−8411.

(78) Winzer, T.; Knorr, A.; Malic, E. Carrier Multiplication in Graphene. *Nano Lett.* **2010**, *10*, 4839−4843.

(79) Plötzing, T.; Winzer, T.; Malic, E.; Neumaier, D.; Knorr, A.; Kurz, H. Experimental Verification of Carrier Multiplication in Graphene. *Nano Lett.* **2014**, *14*, 5371−5375.

(80) Song, J. C. W.; Tielrooij, K. J.; Koppens, F. H. L.; Levitov, L. S. Photoexcited carrier dynamics and impact-excitation cascade in graphene. *Phys. Rev. B* **2013**, *87*, 155429.

(81) Tielrooij, K. J.; Song, J. C. W.; Jensen, S. A.; Centeno, A.; Pesquera, A.; Zurutuza Elorza, A.; Bonn, M.; Levitov, L. S.; Koppens, F. H. L. Photoexcitation cascade and multiple hot-carrier generation in graphene. *Nat. Phys.* **2013**, *9*, 248−252.

(82) Tomadin, A.; Brida, D.; Cerullo, G.; Ferrari, A. C.; Polini, M. Nonequilibrium dynamics of photoexcited electrons in graphene: Collinear scattering, Auger processes, and the impact of screening. *Phys. Rev. B* **2013**, *88*, 035430.

(83) Song, J. C. W.; Levitov, L. S. Energy flows in graphene: hot carrier dynamics and cooling. *J. Phys.: Condens. Matter* **2015**, *27*, 164201.

(84) Urich, A.; Unterrainer, K.; Mueller, T. Intrinsic Response Time of Graphene Photodetectors. *Nano Lett.* **2011**, *11*, 2804−2808.

(85) Johannsen, J. C.; Ulstrup, S.; Cilento, F.; Crepaldi, A.; Zacchigna, M.; Cacho, C.; Turcu, I. C.; Springate, E.; Fromm, F.; Raidel, C.; Seyller, T.; Parmigiani, F.; Grioni, M.; Hofmann, P. Direct View of Hot Carrier Dynamics in Graphene. *Phys. Rev. Lett.* **2013**, *111*, 027403.

(86) Graham, M. W.; Shi, S.-F.; Ralph, D. C.; Park, J.; McEuen, P. L. Photocurrent measurements of supercollision cooling in graphene. *Nat. Phys.* **2013**, *9*, 103−108.

(87) Tielrooij, K.-J.; et al. Out-of-plane heat transfer in van der Waals stacks through electron-hyperbolic phonon coupling. *Nat. Nanotechnol.* **2018**, *13*, 41−46.

(88) Lazzeri, M.; Piscanec, S.; Mauri, F.; Ferrari, A. C.; Robertson, J. Electron Transport and Hot Phonons in Carbon Nanotubes. *Phys. Rev. Lett.* **2005**, *95*, 236802.

(89) Pogna, E. A. A.; et al. Hot-Carrier Cooling in High-Quality Graphene Is Intrinsically Limited by Optical Phonons. *ACS Nano* **2021**, *15*, 11285−11295.

(90) Pop, E.; Varshney, V.; Roy, A. K. Thermal properties of graphene: Fundamentals and applications. *MRS Bull.* **2012**, *37*, 1273−1281.

(91) Fang, Z.; Wang, Y.; Liu, Z.; Schlather, A.; Ajayan, P. M.; Koppens, F. H. L.; Nordlander, P.; Halas, N. J. Plasmon-Induced Doping of Graphene. *ACS Nano* **2012**, *6*, 10222−10228.

(92) Fang, Z.; Liu, Z.; Wang, Y.; Ajayan, P. M.; Nordlander, P.; Halas, N. J. Graphene-Antenna Sandwich Photodetector. *Nano Lett.* **2012**, *12*, 3808−3813.

(93) Giovannetti, G.; Khomyakov, P. A.; Brocks, G.; Karpan, V. M.; van den Brink, J.; Kelly, P. J. Doping Graphene with Metal Contacts. *Phys. Rev. Lett.* **2008**, *101*, 026803.

(94) Casiraghi, C.; Pisana, S.; Novoselov, K. S.; Geim, A. K.; Ferrari, A. C. Raman fingerprint of charged impurities in graphene. *Appl. Phys. Lett.* **2007**, *91*, 233108.

(95) Rhodes, D.; Chae, S. H.; Ribeiro-Palau, R.; Hone, J. Disorder in van der Waals heterostructures of 2D materials. *Nat. Mater.* **2019**, *18*, 541−549.

(96) Decker, R.; Wang, Y.; Brar, V. W.; Regan, W.; Tsai, H.-Z.; Wu, Q.; Gannett, W.; Zettl, A.; Crommie, M. F. Local Electronic Properties of Graphene on a BN Substrate via Scanning Tunneling Microscopy. *Nano Lett.* **2011**, *11*, 2291−2295.

(97) Sundaram, R. S.; Steiner, M.; Chiu, H.-Y.; Engel, M.; Bol, A. A.; Krupke, R.; Burghard, M.; Kern, K.; Avouris, P. The Graphene-Gold Interface and Its Implications for Nanoelectronics. *Nano Lett.* **2011**, *11*, 3833−3837.

(98) Castilla, S.; Terrés, B.; Autore, M.; Viti, L.; Li, J.; Nikitin, A. Y.; Vangelidis, I.; Watanabe, K.; Taniguchi, T.; Lidorikis, E.; Vitiello, M. S.; Hillenbrand, R.; Tielrooij, K.-J.; Koppens, F. H. L. Fast and Sensitive Terahertz Detection Using an Antenna-Integrated Graphene pn Junction. *Nano Lett.* **2019**, *19*, 2765−2773.

(99) Halbertal, D.; Ben Shalom, M.; Uri, A.; Bagani, K.; Meltzer, A. Y.; Marcus, I.; Myasoedov, Y.; Birkbeck, J.; Levitov, L. S.; Geim, A. K.; Zeldov, E. Imaging resonant dissipation from individual atomic defects in graphene. *Science* **2017**, *358*, 1303−1306.

(100) AlAloul, M.; Rasras, M. Plasmon-enhanced graphene photodetector with CMOS-compatible titanium nitride. *J. Opt. Soc. Am. B* **2021**, *38*, 602−610.

(101) Gosciniak, J.; Rasras, M.; Khurgin, J. B. Ultrafast Plasmonic Graphene Photodetector Based on the Channel Photothermoelectric Effect. *ACS Photonics* **2020**, *7*, 488−498.

(102) Enescu, D. *Green Energy Advances*; Enescu, D., Ed.; IntechOpen: Rijeka, 2019, Chapter 1.

(103) Soavi, G.; et al. Broadband, electrically tunable third-harmonic generation in graphene. *Nat. Nanotechnol.* **2018**, *13*, 583−588.

(104) Cheng, F. *Thermoelectrics for Power Generation*; Skipidarov, S., Nikitin, M., Eds.; IntechOpen: Rijeka, 2016, Chapter 19.

(105) Saavedra, J. R. M.; Asenjo-Garcia, A.; García de Abajo, F. J. Hot-Electron Dynamics and Thermalization in Small Metallic Nanoparticles. *ACS Photonics* **2016**, *3*, 1637−1646.

(106) Liu, J. G.; Zhang, H.; Link, S.; Nordlander, P. Relaxation of Plasmon-Induced Hot Carriers. *ACS Photonics* **2018**, *5*, 2584−2595.

(107) Fann, W. S.; Storz, R.; Tom, H. W. K.; Bokor, J. Electron thermalization in gold. *Phys. Rev. B* **1992**, *46*, 13592−13595.

(108) Sun, C.-K.; Vallée, F.; Acioli, L. H.; Ippen, E. P.; Fujimoto, J. G. Femtosecond-tunable measurement of electron thermalization in gold. *Phys. Rev. B* **1994**, *50*, 15337−15348.

(109) Link, S.; El-Sayed, M. A. Spectral Properties and Relaxation Dynamics of Surface Plasmon Electronic Oscillations in Gold and Silver Nanodots and Nanorods. *J. Phys. Chem. B* **1999**, *103*, 8410−8426.

(110) Voisin, C.; Christofilos, D.; Loukakos, P. A.; Del Fatti, N.; Vallée, F.; Lermé, J.; Gaudry, M.; Cottancin, E.; Pellarin, M.; Broyer, M. Ultrafast electron-electron scattering and energy exchanges in noble-metal nanoparticles. *Phys. Rev. B* **2004**, *69*, 195416.

(111) Dowgiallo, A.-M.; Knappenberger, K. L. Ultrafast electron-phonon coupling in hollow gold nanospheres. *Phys. Chem. Chem. Phys.* **2011**, *13*, 21585−21592.

(112) Casiraghi, C. Probing disorder and charged impurities in graphene by Raman spectroscopy. *Phys. Status Solidi RRL* **2009**, *3*, 175−177.

(113) Couto, N. J. G.; Costanzo, D.; Engels, S.; Ki, D.-K.; Watanabe, K.; Taniguchi, T.; Stampfer, C.; Guinea, F.; Morpurgo, A. F. Random Strain Fluctuations as Dominant Disorder Source for High-Quality On-Substrate Graphene Devices. *Phys. Rev. X* **2014**, *4*, 041019.

(114) Fang, T.; Konar, A.; Xing, H.; Jena, D. Carrier statistics and quantum capacitance of graphene sheets and ribbons. *Appl. Phys. Lett.* **2007**, *91*, 092109.

(115) Kim, K. K.; Hsu, A.; Jia, X.; Kim, S. M.; Shi, Y.; Dresselhaus, M.; Palacios, T.; Kong, J. Synthesis and Characterization of Hexagonal Boron Nitride Film as a Dielectric Layer for Graphene Devices. *ACS Nano* **2012**, *6*, 8583−8590.

(116) Hoggard, A.; Wang, L.-Y.; Ma, L.; Fang, Y.; You, G.; Olson, J.; Liu, Z.; Chang, W.-S.; Ajayan, P. M.; Link, S. Using the Plasmon Linewidth To Calculate the Time and Efficiency of Electron Transfer between Gold Nanorods and Graphene. *ACS Nano* **2013**, *7*, 11209−11217.

(117) Brongersma, M. L.; Halas, N. J.; Nordlander, P. Plasmon-induced hot carrier science and technology. *Nat. Nanotechnol.* **2015**, *10*, 25−34.

(118) Lumerical Inc.. https://www.lumerical.com/products/fdtd/ (accessed Feb 06, 2021).

(119) Johnson, P. B.; Christy, R. W. Optical Constants of the Noble Metals. *Phys. Rev. B* **1972**, *6*, 4370−4379.

(120) Woessner, A.; Lundeberg, M. B.; Gao, Y.; Principi, A.; Alonso-González, P.; Carrega, M.; Watanabe, K.; Taniguchi, T.; Vignale, G.; Polini, M.; Hone, J.; Hillenbrand, R.; Koppens, F. H. L. Highly confined low-loss plasmons in graphene-boron nitride heterostructures. *Nat. Mater.* **2015**, *14*, 421−425.

(121) Kischkat, J.; Peters, S.; Gruska, B.; Semtsiv, M.; Chashnikova, M.; Klinkmüller, M.; Fedosenko, O.; Machulik, S.; Aleksandrova, A.; Monastyrskyi, G.; Flores, Y.; Ted Masselink, W. Mid-infrared optical properties of thin films of aluminum oxide, titanium dioxide, silicon dioxide, aluminum nitride, and silicon nitride. *Appl. Opt.* **2012**, *51*, 6789−6798.

(122) Hanson, G. W. Quasi-transverse electromagnetic modes supported by a graphene parallel-plate waveguide. *J. Appl. Phys.* **2008**, *104*, 084314.

(123) Luo, F.; et al. Graphene Thermal Emitter with Enhanced Joule Heating and Localized Light Emission in Air. *ACS Photonics* **2019**, *6*, 2117−2125.

(124) Grosse, K. L.; Bae, M.-H.; Lian, F.; Pop, E.; King, W. P. Nanoscale Joule heating, Peltier cooling and current crowding at graphene-metal contacts. *Nat. Nanotechnol.* **2011**, *6*, 287−290.

(125) Andersen, T. I.; Smith, T. B.; Principi, A. Enhanced Photoenergy Harvesting and Extreme Thomson Effect in Hydrodynamic Electronic Systems. *Phys. Rev. Lett.* **2019**, *122*, 166802.

(126) Fang, Y.; Armin, A.; Meredith, P.; Huang, J. Accurate characterization of next-generation thin-film photodetectors. *Nat. Photonics* **2019**, *13*, 1−4.

(127) Guo, Q.; Yu, R.; Li, C.; Yuan, S.; Deng, B.; García de Abajo, F. J.; Xia, F. Efficient electrical detection of mid-infrared graphene plasmons at room temperature. *Nat. Mater.* **2018**, *17*, 986−992.

(128) Balandin, A. A. Low-frequency 1/f noise in graphene devices. *Nat. Nanotechnol.* **2013**, *8*, 549−555.

(129) Tan, Y.-W.; Zhang, Y.; Bolotin, K.; Zhao, Y.; Adam, S.; Hwang, E. H.; Das Sarma, S.; Stormer, H. L.; Kim, P. Measurement of Scattering Rate and Minimum Conductivity in Graphene. *Phys. Rev. Lett.* **2007**, *99*, 246803.

(130) Zuev, Y. M.; Chang, W.; Kim, P. Thermoelectric and Magnetothermoelectric Transport Measurements of Graphene. *Phys. Rev. Lett.* **2009**, *102*, 096807.

(131) Cutler, M.; Mott, N. F. Observation of Anderson Localization in an Electron Gas. *Phys. Rev.* **1969**, *181*, 1336−1340.

(132) Jones, W.; March, N. *Theoretical Solid State Physics: Perfect Lattices in Equilibrium*; Dover Books on Physics Series; Dover Publications, 1985.

(133) Young, A. F.; Dean, C. R.; Meric, I.; Sorgenfrei, S.; Ren, H.; Watanabe, K.; Taniguchi, T.; Hone, J.; Shepard, K. L.; Kim, P. Electronic compressibility of layer-polarized bilayer graphene. *Phys. Rev. B* **2012**, *85*, 235458.

(134) Duan, J.; Wang, X.; Lai, X.; Li, G.; Watanabe, K.; Taniguchi, T.; Zebarjadi, M.; Andrei, E. Y. High thermoelectricpower factor in graphene/hBN devices. *Proc. Natl. Acad. Sci. U.S.A.* **2016**, *113*, 14272−14276.